Kinetic Energy Flow Instability With Application to Couette Flow

L. Ridgway Scott
University of Chicago

July 27, 2023

Abstract

We examine a definition of instability for steady flows based on kinetic energy which originated with Reynolds and Orr [37]. Using this definition, we compute the most unstable mode for Couette flow. We find that instability occurs above a Reynolds number of about 177. The usual eigenvalue (linear) stability analysis predicts that there is no instability of Couette flow for any Reynolds number. So the kinetic energy criterion for instability gives a prediction more in accord with experimental evidence. We demonstrate the effect of the perturbation on time-dependent flows. For Reynolds numbers below the critical value, perturbations decay. For Reynolds numbers above the critical value, perturbations grow initially but in all cases studied they eventually decay to zero. However, the maximum amplitude and the persistence time of the perturbations both increase with Reynolds number in all cases studied.

Stability of fluid flow is the subject of many books [6, 15, 18, 19, 24, 31, 34]. Yet standard theoretical (linear) stability analysis of the simplest flow problems, such as Couette flow, has caused significant confusion, since it predicts [32, 3] that Couette flow is stable for all Reynolds numbers, something that is contrary to experimental evidence [9, 40, 30, 43]. In particular [17, Section 9.3], the standard approximate, linear stability analysis for Couette flow leads to an eigenproblem for a nonnormal linear system. This fact has stimulated novel approaches [41, 42, 11] to interpret the linear algebra.

We advocate here a nonlinear analysis [37, 34], with no approximations, which nevertheless leads to a (very well posed) symmetric linear eigenproblem and a precise condition for (kinetic energy) instability for Reynolds numbers larger than a critical value associated (nonlinearly) with the corresponding eigenvalue. We show in Section 9.2 that all instabilities found by the standard approach are also found in the nonlinear analysis, for any flow problem. The converse is false as indicated by Couette flow.

Couette flow has been of significant interest for many years [28, 39]. Moreover, in many ways it is the simplest possible flow problem. Thus it is quite surprising that understanding of the stability or instability of Couette flow has been equivocal. We do not elaborate on a possible explanation here, but it is of note that the approach taken here is standard in the

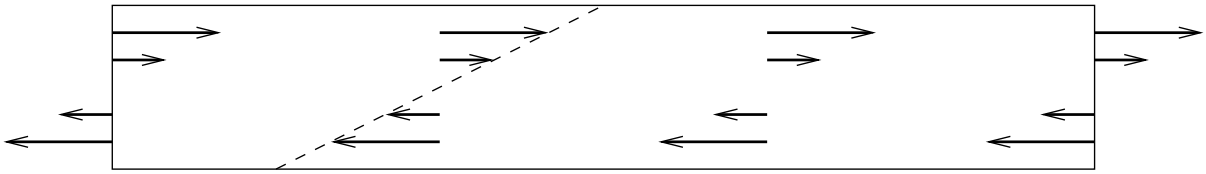

Figure 1: Couette flow in a channel.

variational theory of partial differential equations, whose genesis is in the work of Banach and Hilbert. By contrast, the standard notions of linear stability analysis, for which Couette flow appears incorrectly to be stable for all Reynolds numbers, has its roots in much earlier approaches to differential equations, say, the time of Euler or even earlier.

The kinetic energy assessment of stability has been widely known for some time, utilized by Serrin [37] in work published in 1959. Serrin gives a list of references that also use this analysis, going back to the original work of Reynolds and Orr but including other intervening work as well. Perhaps the paper [37] did not have more impact on subsequent research on instability because Serrin was more focused on stability than instability, and because computational resources in 1959 would have made it difficult to determine unstable modes and their evolution with accuracy.

Flow complexity can grow in two ways, one via bifurcations [7] and the other through instability [20]. The former occurs, for example, in flow in a channel with a sudden expansion [36, Section 21.3]. The latter refers to the impact of small perturbations on the global flow. Many models have been proposed for the definition of stability and instability [10]. Here we use a way [37, 34] to measure instability that is not an approximation in any way. We review this approach in the following. See [22] for a recent study using this approach.

1 Couette flow

Suppose that $(\mathbf{u}, p)$ is a solution of the Navier-Stokes equations

$$\begin{gathered} R\,\mathbf{u}_t - \Delta\mathbf{u} + R\,\mathbf{u}\cdot\nabla\mathbf{u} + \nabla p = \mathbf{0} \text{ in } \Omega, \\ \nabla\cdot\,\mathbf{u} = 0 \text{ in } \Omega, \quad \mathbf{u} = \mathbf{g} \text{ on } \partial\Omega, \end{gathered} \tag{1}$$

in a domain Ω and for $t \in [0, T]$, where R is the Reynolds number. The physical pressure has been scaled by the Reynolds number R, but this scaling plays no role here. We assume initial conditions $\mathbf{u}(\mathbf{x}, 0) = \mathbf{u}_0(\mathbf{x})$ for $\mathbf{x} \in \Omega$.

By Couette flow, we mean flow in a domain defined by

$$\Omega = \{(x, y) \ : \ |x| \le L, \ 0 \le y \le 1\}\,. \tag{2}$$

In section 11, we will consider extending this to three dimensions. The boundary conditions for Couette flow are given by

$$\mathbf{g}(x, y, t) = (y - \tfrac{1}{2}, 0)^t \tag{3}$$

for all $(x, y) \in \mathbb{R}^2$. Thus the flow rate is linear, and it has a nonzero component only in the x direction. The extension of this to three dimensions is to make $\mathbf{g}$ constant in z.

The solution of (1) is $\mathbf{u} = \mathbf{g}$ for all t, with $p = 0$, as can easily be verified. In particular, the first two terms in (1) are both zero. The nonlinear term has to be checked more carefully, but

$$\mathbf{g} \cdot \nabla \mathbf{g} = g_x(\mathbf{g}_{,x}) + g_y(\mathbf{g}_{,y}) = (y - \tfrac{1}{2})\mathbf{0} + 0(\mathbf{g}_{,y}) = \mathbf{0}.$$

One significant observation is that the solution does not depend on R. The velocity $\mathbf{u}$ is depicted in Figure 1.

2 Flow instability

Now we consider the stability of solutions of (1) for general domains Ω in two or three dimensions. Suppose that $(\mathbf{w}, q)$ is another solution of the Navier-Stokes equations

$$\begin{aligned} R\mathbf{w}_t - \Delta \mathbf{w} + R\,\mathbf{w} \cdot \nabla \mathbf{w} + \nabla q = \mathbf{0} \text{ in } \Omega, \\ \nabla \cdot \mathbf{w} = 0 \text{ in } \Omega, \quad \mathbf{w} = \mathbf{g} \text{ on } \partial\Omega, \end{aligned} \tag{4}$$

together with initial conditions $\mathbf{w}(\mathbf{x}, 0) = \mathbf{w}_0(\mathbf{x})$ for $\mathbf{x} \in \Omega$.

Suppose that the only difference between $\mathbf{u}$ and $\mathbf{w}$ is that they differ slightly at $t = 0$: $\mathbf{v}_0 = \mathbf{u}_0 - \mathbf{w}_0 \neq \mathbf{0}$. If we define $\mathbf{v}$ for all time by

$$\mathbf{v} = \mathbf{u} - \mathbf{w},$$

then we see that $\mathbf{v}$ solves the equations

$$\begin{aligned} R\mathbf{v}_t - \Delta \mathbf{v} + R\big(\mathbf{u} \cdot \nabla \mathbf{u} - \mathbf{w} \cdot \nabla \mathbf{w}\big) + \nabla o = \mathbf{0} \text{ in } \Omega, \\ \nabla \cdot \mathbf{v} = 0 \text{ in } \Omega, \quad \mathbf{v} = \mathbf{0} \text{ on } \partial\Omega, \end{aligned} \tag{5}$$

where $o = p - q$ and $\mathbf{v}(t = 0) = \mathbf{v}_0 = \mathbf{u}_0 - \mathbf{w}_0$. But

$$\begin{aligned} \mathbf{u} \cdot \nabla \mathbf{u} - \mathbf{w} \cdot \nabla \mathbf{w} &= \mathbf{u} \cdot \nabla \mathbf{u} - \mathbf{u} \cdot \nabla \mathbf{w} + \mathbf{u} \cdot \nabla \mathbf{w} - \mathbf{w} \cdot \nabla \mathbf{w} = \mathbf{u} \cdot \nabla \mathbf{v} + \mathbf{v} \cdot \nabla \mathbf{w} \\ &= \mathbf{u} \cdot \nabla \mathbf{v} + \mathbf{v} \cdot \nabla (\mathbf{u} - \mathbf{v}) = \mathbf{u} \cdot \nabla \mathbf{v} + \mathbf{v} \cdot \nabla \mathbf{u} - \mathbf{v} \cdot \nabla \mathbf{v}. \end{aligned} \tag{6}$$

Thus the first equation in (5) becomes

$$R\mathbf{v}_t - \Delta \mathbf{v} + R\big(\mathbf{u} \cdot \nabla \mathbf{v} + \mathbf{v} \cdot \nabla \mathbf{u} - \mathbf{v} \cdot \nabla \mathbf{v}\big) + \nabla o = \mathbf{0} \text{ in } \Omega. \tag{7}$$

3 An exact nonlinear bound

Multiplying equation (7) by $\mathbf{v}$, integrating over Ω, and integrating by parts gives

$$\frac{R}{2}\frac{d}{dt}\int_\Omega |\mathbf{v}|^2\, d\mathbf{x} + \int_\Omega |\nabla \mathbf{v}|^2\, d\mathbf{x} + R\big(c(\mathbf{u}, \mathbf{v}, \mathbf{v}) + c(\mathbf{v}, \mathbf{u}, \mathbf{v}) - c(\mathbf{v}, \mathbf{v}, \mathbf{v})\big) = 0,$$

where

$$c(\mathbf{u},\mathbf{v},\mathbf{w}) = \int_\Omega (\mathbf{u}\cdot\nabla\mathbf{v})\cdot\mathbf{w}\,d\mathbf{x}. \tag{8}$$

It is well known [36, Section 20.1.1], that

$$c(\mathbf{u},\mathbf{v},\mathbf{w}) = -c(\mathbf{u},\mathbf{w},\mathbf{v}), \qquad c(\mathbf{u},\mathbf{v},\mathbf{v}) = 0, \qquad c(\mathbf{v},\mathbf{v},\mathbf{v}) = 0, \tag{9}$$

since $\mathbf{u}$, $\mathbf{v}$, and $\mathbf{w}$ are divergence free and $\mathbf{v}$ vanishes on $\partial\Omega$. Moreover

$$c(\mathbf{v},\mathbf{u},\mathbf{v}) = \int_\Omega (\mathbf{v}\cdot\nabla\mathbf{u})\cdot\mathbf{v}\,d\mathbf{x} = \int_\Omega \mathbf{v}^t(\nabla\mathbf{u})\mathbf{v}\,d\mathbf{x} = \frac{1}{2}\int_\Omega \mathbf{v}^t\big(\nabla\mathbf{u}+\nabla\mathbf{u}^t\big)\mathbf{v}\,d\mathbf{x}.$$

Thus we find

$$\frac{R}{2}\frac{d}{dt}\int_\Omega |\mathbf{v}|^2\,d\mathbf{x} = -\int_\Omega |\nabla\mathbf{v}|^2\,d\mathbf{x} - \frac{R}{2}\int_\Omega \mathbf{v}^t(\nabla\mathbf{u}+\nabla\mathbf{u}^t)\mathbf{v}\,d\mathbf{x}. \tag{10}$$

The kinetic energy relation (10) can be found in [37, (4)] and [34, Section 5.6.1].

For all $\mathbf{x}\in\Omega$ and $t\in[0,T]$, the matrix $\mathbf{B}(\mathbf{x},t)$ defined by

$$\mathbf{B}(\mathbf{x},t) = \nabla\mathbf{u}(\mathbf{x},t) + \nabla\mathbf{u}(\mathbf{x},t)^t$$

is symmetric and has trace zero. Thus we expect that $\mathbf{B}(\mathbf{x},t)$ will have eigenvalues of both signs, and in particular it might happen that

$$-\int_\Omega |\nabla\mathbf{v}_0|^2\,d\mathbf{x} - \frac{R}{2}\int_\Omega \mathbf{v}_0^t\big(\nabla\mathbf{u}_0+\nabla\mathbf{u}_0^t\big)\mathbf{v}_0\,d\mathbf{x} > 0, \tag{11}$$

in which case $\|\mathbf{v}\|_{L^2(\Omega)}$ would initially increase. This suggests a criterion for stability.

4 Definition of energy instability

If there exists $\mathbf{v}_0\in H^1(\Omega)^d$ that

1. $\nabla\cdot\mathbf{v}_0 = 0$ in Ω,
2. $\mathbf{v}_0 = \mathbf{0}$ on $\partial\Omega$, and
3. $-\frac{1}{2}R\int_\Omega \mathbf{v}_0^t(\nabla\mathbf{u}_0+\nabla\mathbf{u}_0^t)\mathbf{v}_0\,d\mathbf{x} > \int_\Omega |\nabla\mathbf{v}_0|^2\,d\mathbf{x}$,

then we say the flow is *energy unstable* at $t=0$, motivated by the terminology in [34, Section 5.6]. Define the space V of divergence-free, vector-valued functions that vanish on the boundary and are in the Sobolev space $H^1(\Omega)^d$, that is

$$V = V^d = \left\{\mathbf{v}\in H^1(\Omega)^d \;:\; \nabla\cdot\mathbf{v} = 0 \text{ in } \Omega,\ \mathbf{v} = \mathbf{0} \text{ on } \partial\Omega\right\}. \tag{12}$$

When necessary, we will write V^d to indicate the dimension of Ω in the definition (12), but otherwise we will assume that the dimension is implicit. In this case, the superscript is just that, not the power in a Cartesian product as it is for $H^1(\Omega)^d$. In general, we will omit the superscript on V.

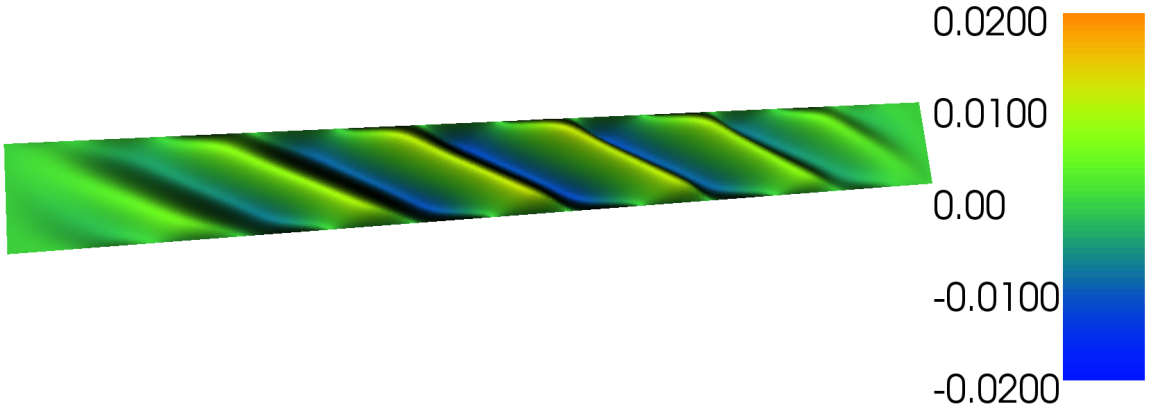

Figure 2: Horizontal flow component of the most unstable mode for Couette flow, computed on the domain (2) with meshsize parameter $M = 128$ and 700 iterations of the power method with $\mu = 0.01$: $L = 5$, $\lambda = -0.01122$. The meshsize parameter M is explained in section 8.7. Initial eigenvector approximation is $(0, 1)$.

Definition 4.1 *We say that the flow* $\mathbf{u}$ *is* energy unstable *at* $t = 0$ *for Reynolds number* R *if*

$$-\inf_{\mathbf{0}\neq\mathbf{v}\in V} \frac{\int_\Omega \mathbf{v}^t(\nabla\mathbf{u}_0 + \nabla\mathbf{u}_0^t)\mathbf{v}\,d\mathbf{x}}{\int_\Omega |\nabla\mathbf{v}|^2\,d\mathbf{x}} = \sup_{\mathbf{0}\neq\mathbf{v}\in V} -\frac{\int_\Omega \mathbf{v}^t(\nabla\mathbf{u}_0 + \nabla\mathbf{u}_0^t)\mathbf{v}\,d\mathbf{x}}{\int_\Omega |\nabla\mathbf{v}|^2\,d\mathbf{x}} > \frac{2}{R}. \tag{13}$$

If by chance

$$\inf_{\mathbf{0}\neq\mathbf{v}\in V} \frac{\int_\Omega \mathbf{v}^t(\nabla\mathbf{u}_0 + \nabla\mathbf{u}_0^t)\mathbf{v}\,d\mathbf{x}}{\int_\Omega |\nabla\mathbf{v}|^2\,d\mathbf{x}} \geq 0,$$

then the flow is energy stable for all Reynolds numbers R. On the other hand, if (13) holds, it means there is some $\mathbf{v}_0$ that leads to instability.

5 Most unstable mode

The parameter λ defined by

$$\lambda = \inf_{\mathbf{0}\neq\mathbf{v}\in V} \frac{\int_\Omega \mathbf{v}^t(\nabla\mathbf{u}_0 + \nabla\mathbf{u}_0^t)\mathbf{v}\,d\mathbf{x}}{\int_\Omega |\nabla\mathbf{v}|^2\,d\mathbf{x}}$$

can be identified as a generalized eigenvalue, as follows. Let us introduce some notation involving bilinear forms:

$$a(\mathbf{u}, \mathbf{v}) = \int_\Omega \nabla\mathbf{u} : \nabla\mathbf{v}\,d\mathbf{x}, \qquad \mathcal{B}_\mathbf{u}(\mathbf{v}, \mathbf{w}) = \int_\Omega \mathbf{v}^t(\nabla\mathbf{u} + \nabla\mathbf{u}^t)\mathbf{w}\,d\mathbf{x}. \tag{14}$$

Then

$$\lambda = \inf_{\mathbf{0}\neq\mathbf{v}\in V} \frac{\mathcal{B}_{\mathbf{u}}(\mathbf{v},\mathbf{v})}{a(\mathbf{v},\mathbf{v})}, \tag{15}$$

where we have dropped the subscript 0 on $\mathbf{u}$ for the moment. First, let us develop some bounds on this minimization problem.

5.1 Limits on λ

We can give some bounds on the values of λ in (15). Recall the Poincaré inequality [36]

$$\int_\Omega |\mathbf{v}|^2 \, d\mathbf{x} \leq c_P \int_\Omega |\nabla \mathbf{v}|^2 \, d\mathbf{x} = c_P \, a(\mathbf{v},\mathbf{v}), \tag{16}$$

valid for all $\mathbf{v} \in V$. Then

$$\begin{aligned} \big|\mathcal{B}_{\mathbf{u}}(\mathbf{v},\mathbf{v})\big| &\leq 2 \sup_{\mathbf{x}\in\Omega} \|\nabla \mathbf{u}(\mathbf{x})\|_F \int_\Omega |\mathbf{v}|^2 \, d\mathbf{x} \\ &\leq 2\, c_P \sup_{\mathbf{x}\in\Omega} \|\nabla \mathbf{u}(\mathbf{x})\|_F \, a(\mathbf{v},\mathbf{v}), \end{aligned} \tag{17}$$

where $\|\cdot\|_F$ denotes the Frobenius norm. Thus any minimizer λ of (15) must satisfy

$$|\lambda| \leq 2\, c_P \sup_{\mathbf{x}\in\Omega} \|\nabla \mathbf{u}(\mathbf{x})\|_F. \tag{18}$$

We will give an explicit bound on c_P for Couette flow in Section 6.1.

5.2 Eigenproblem derivation

Suppose that λ is a minimum of (15) and that $\mathbf{v} \in V$ satisfies

$$\mathcal{B}_{\mathbf{u}}(\mathbf{v},\mathbf{v}) = \lambda \, a(\mathbf{v},\mathbf{v}).$$

Let $\epsilon > 0$ and $\mathbf{w} \in V$. Then

$$\frac{\mathcal{B}_{\mathbf{u}}(\mathbf{v}+\epsilon\mathbf{w},\mathbf{v}+\epsilon\mathbf{w})}{a(\mathbf{v}+\epsilon\mathbf{w},\mathbf{v}+\epsilon\mathbf{w})} \geq \lambda \implies \mathcal{B}_{\mathbf{u}}(\mathbf{v}+\epsilon\mathbf{w},\mathbf{v}+\epsilon\mathbf{w}) \geq \lambda a(\mathbf{v}+\epsilon\mathbf{w},\mathbf{v}+\epsilon\mathbf{w}),$$

and this holds for all $\epsilon > 0$ and $\mathbf{w} \in V$. Expanding, we find

$$\begin{aligned} \mathcal{B}_{\mathbf{u}}(\mathbf{v},\mathbf{v}) + 2\epsilon\mathcal{B}_{\mathbf{u}}(\mathbf{v},\mathbf{w}) + \epsilon^2\mathcal{B}_{\mathbf{u}}(\mathbf{w},\mathbf{w}) &\geq \lambda\big(a(\mathbf{v},\mathbf{v}) + 2\epsilon a(\mathbf{v},\mathbf{w}) + \epsilon^2 a(\mathbf{w},\mathbf{w})\big) \\ &= \mathcal{B}_{\mathbf{u}}(\mathbf{v},\mathbf{v}) + \lambda\big(2\epsilon a(\mathbf{v},\mathbf{w}) + \epsilon^2 a(\mathbf{w},\mathbf{w})\big). \end{aligned} \tag{19}$$

Subtracting $\mathcal{B}_{\mathbf{u}}(\mathbf{v},\mathbf{v})$ from both sides and dividing by 2ϵ gives

$$\mathcal{B}_{\mathbf{u}}(\mathbf{v},\mathbf{w}) + \tfrac{1}{2}\epsilon\mathcal{B}_{\mathbf{u}}(\mathbf{w},\mathbf{w}) \geq \lambda\big(a(\mathbf{v},\mathbf{w}) + \tfrac{1}{2}\epsilon a(\mathbf{w},\mathbf{w})\big).$$

Letting $\epsilon \to 0$, we find

$$\mathcal{B}_{\mathbf{u}}(\mathbf{v},\mathbf{w}) \geq \lambda a(\mathbf{v},\mathbf{w})$$

for all $\mathbf{w} \in V$. But taking $\mathbf{z} = -\mathbf{w}$, we also find

$$-\mathcal{B}_{\mathbf{u}}(\mathbf{v}, \mathbf{w}) = \mathcal{B}_{\mathbf{u}}(\mathbf{v}, \mathbf{z}) \geq \lambda a(\mathbf{v}, \mathbf{z}) = -\lambda a(\mathbf{v}, \mathbf{w}),$$

so that we also have

$$\mathcal{B}_{\mathbf{u}}(\mathbf{v}, \mathbf{w}) \leq \lambda a(\mathbf{v}, \mathbf{w}).$$

Thus we must have

$$\mathcal{B}_{\mathbf{u}}(\mathbf{v}, \mathbf{w}) = \lambda a(\mathbf{v}, \mathbf{w}), \tag{20}$$

for all $\mathbf{w} \in V$.

What this shows is that if $\mathbf{v}$ is a minimizer of (15), then it solves the eigenproblem (20). Conversely, if $\widehat{\mathbf{v}}$ is any solution of (20), then

$$\frac{\mathcal{B}_{\mathbf{u}}(\widehat{\mathbf{v}}, \widehat{\mathbf{v}})}{a(\widehat{\mathbf{v}}, \widehat{\mathbf{v}})} = \frac{\lambda a(\widehat{\mathbf{v}}, \widehat{\mathbf{v}})}{a(\widehat{\mathbf{v}}, \widehat{\mathbf{v}})} = \lambda.$$

Thus $\widehat{\mathbf{v}}$ is a minimizer of (15).

5.3 Eigenproblem computation

The solution of (20) can be approximated variationally via: find $\mathbf{v}_\lambda \in V_h$ such that

$$a(\mathbf{v}_\lambda, \mathbf{w}) = \lambda^{-1} \mathcal{B}_{\mathbf{u}}(\mathbf{v}_\lambda, \mathbf{w}) \quad \forall \mathbf{w} \in V_h, \tag{21}$$

where $V_h \subset V$ and V is the subset of $H^1(\Omega)^d$ consisting of divergence-free functions vanishing on the boundary, defined in (12). We can write this in operator form as

$$\lambda \mathbf{v}_\lambda = A^{-1} B \mathbf{v}_\lambda. \tag{22}$$

Here, the operator $A : V_h \to V_h$ is defined by

$$(A\mathbf{v}, \mathbf{w})_{L^2} = a(\mathbf{v}, \mathbf{w}), \qquad \forall \mathbf{w} \in V_h.$$

The operator $B : V_h \to V_h$ can be defined as the multiplication operator by the function $\mathbf{B} = \nabla \mathbf{u}_0 + \nabla \mathbf{u}_0^t$, followed by the L^2 projection onto V_h. Then the operator B also satisfies

$$(B\mathbf{v}, \mathbf{w})_{L^2} = \mathcal{B}_{\mathbf{u}}(\mathbf{v}, \mathbf{w}), \qquad \forall \mathbf{w} \in V_h.$$

Note that the functions of the form $B\mathbf{v}$ are not necessarily divergence free.

We can number the eigenvalues $\lambda_0 \leq \lambda_1 \leq \cdots$. Some of these are potentially negative. The power method targets the eigenvector whose eigenvalue is largest in magnitude. Since we seek the most negative eigenvalue, we must make a shift so that appears to be the largest in magnitude. So consider the shifted eigenproblem

$$\lambda^\mu \mathbf{v} = (A^{-1} B - \mu I)\mathbf{v}. \tag{23}$$

Then the eigenvalues for this problem are

$$\lambda_0^\mu \le \lambda_1^\mu \le \cdots = \lambda_0 - \mu \le \lambda_1 - \mu \le \cdots .$$

Using (18), we can choose $\mu \ge 0$ so that all of the eigenvalues $\lambda_i^\mu < 0$.

The power method iteration for solving (23) can be written in operator form as

$$A\mathbf{v}^k = (B - \mu A)\widehat{\mathbf{v}}^{k-1}, \qquad \widehat{\mathbf{v}}^k = \|\mathbf{v}^k\|_{L^2}^{-1}\mathbf{v}^k, \qquad \lambda_k^\mu = \frac{((A^{-1}B - \mu I)\mathbf{v}^k, \mathbf{v}^k)_{L^2}}{(\mathbf{v}^k, \mathbf{v}^k)_{L^2}}, \tag{24}$$

and we expect this to converge to the eigenvector corresponding to the largest (in magnitude) eigenvalue of $A^{-1}(B - \mu A)$ [35].

We can unravel the Rayleigh quotient as follows. We have

$$\begin{aligned}\frac{((A^{-1}B - \mu I)\mathbf{v}^k, \mathbf{v}^k)_{L^2}}{(\mathbf{v}^k, \mathbf{v}^k)_{L^2}} &= \frac{((A^{-1}B)\mathbf{v}^k, \mathbf{v}^k)_{L^2}}{(\mathbf{v}^k, \mathbf{v}^k)_{L^2}} + \frac{((-\mu I)\mathbf{v}^k, \mathbf{v}^k)_{L^2}}{(\mathbf{v}^k, \mathbf{v}^k)_{L^2}} \\ &= \frac{((A^{-1}B)\mathbf{v}^k, \mathbf{v}^k)_{L^2}}{(\mathbf{v}^k, \mathbf{v}^k)_{L^2}} - \mu = \frac{(B\mathbf{v}^k, A^{-1}\mathbf{v}^k)_{L^2}}{(A\mathbf{v}^k, A^{-1}\mathbf{v}^k)_{L^2}} - \mu \\ &= \frac{\mathcal{B}_{\mathbf{u}}(\mathbf{v}^k, A^{-1}\mathbf{v}^k)}{a(\mathbf{v}^k, A^{-1}\mathbf{v}^k)} - \mu.\end{aligned} \tag{25}$$

Thus the unshifted eigenvalue iterates satisfy

$$\lambda_k = \frac{\mathcal{B}_{\mathbf{u}}(\mathbf{v}^k, A^{-1}\mathbf{v}^k)}{a(\mathbf{v}^k, A^{-1}\mathbf{v}^k)}.$$

Computationally, it may be easier to evaluate λ_k^μ as follows. We have

$$\mathbf{v}^k = (A^{-1}B - \mu I)\widehat{\mathbf{v}}^{k-1} = \|\mathbf{v}^{k-1}\|_{L^2}^{-1}(A^{-1}B - \mu I)\mathbf{v}^{k-1}. \tag{26}$$

Turning this around, we have

$$(A^{-1}B - \mu I)\mathbf{v}^{k-1} = \|\mathbf{v}^{k-1}\|_{L^2}\mathbf{v}^k. \tag{27}$$

Increasing indices by 1, we get

$$(A^{-1}B - \mu I)\mathbf{v}^k = \|\mathbf{v}^k\|_{L^2}\mathbf{v}^{k+1}. \tag{28}$$

Thus

$$\lambda_k^\mu = \frac{\|\mathbf{v}^k\|_{L^2}(\mathbf{v}^{k+1}, \mathbf{v}^k)_{L^2}}{(\mathbf{v}^k, \mathbf{v}^k)_{L^2}} = \frac{(\mathbf{v}^{k+1}, \mathbf{v}^k)_{L^2}}{\|\mathbf{v}^k\|_{L^2}} = (\mathbf{v}^{k+1}, \widehat{\mathbf{v}}^k)_{L^2},$$

and so

$$\lambda_k = (\mathbf{v}^{k+1}, \widehat{\mathbf{v}}^k)_{L^2} + \mu. \tag{29}$$

Therefore the only ingredients that must be used to compute the eigenvalue approximation are already defined in the first two steps of (24).

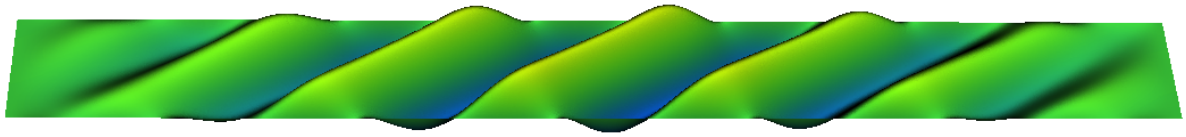

Figure 3: Horizontal flow component of the most stable mode for Couette flow, computed on the domain (2) with meshsize parameter $M = 256$ and 200 iterations of the power method with $\mu = -0.01$: $L = 5$, $\lambda = 0.01122$. The meshsize parameter M is explained in section 8.7. Initial eigenvector approximation was given by (42) with the default frequency $\omega = 3.77$.

In variational form, the first equation in (24) reads: find $\mathbf{v}^k \in V_h$ such that

$$a(\mathbf{v}^k, \mathbf{w}) = \mathcal{B}_{\mathbf{u}}(\widehat{\mathbf{v}}^{k-1}, \mathbf{w}) - \mu\, a(\widehat{\mathbf{v}}^{k-1}, \mathbf{w}) \quad \forall \mathbf{w} \in V_h. \tag{30}$$

This can be implemented by various techniques. In the computations reported in Section 6, we have used the Scott-Vogelius method [36] with quartic Lagrange elements together with the iterated-penalty method to enforce the divergence constraint.

For $\mathbf{v}^0$, we need to pick a function with a non-zero component in the direction of $\mathbf{v}_\lambda$. We refer to this as the *initial eigenvector approximation* in the figure captions.

We can also compute the most positive eigenvalue of (22), by choosing the shift μ to be sufficiently negative. Figure 3 shows the most stable perturbation for $L = 5$ for Couette flow, computed using $\mu = -0.01$. It is noteworthy that the perturbations waves run in opposite directions, but otherwise look essentially identical to the most unstable mode. In addition, it is interesting that in experiments, waves in both directions are seen [30, Figure 3].

5.4 Rate of growth of instability

From (10), we know that

$$\frac{\frac{R}{2}\frac{d}{dt}\int_\Omega |\mathbf{v}|^2\, d\mathbf{x}}{\int_\Omega |\nabla \mathbf{v}|^2\, d\mathbf{x}} = -1 - \frac{R}{2}\frac{\int_\Omega \mathbf{v}^t(\nabla \mathbf{u}_0 + \nabla \mathbf{u}_0^t)\mathbf{v}\, d\mathbf{x}}{\int_\Omega |\nabla \mathbf{v}|^2\, d\mathbf{x}} = -1 - \frac{R\lambda}{2}, \tag{31}$$

at $t = 0$. Therefore, at $t = 0$,

$$\frac{d}{dt}\int_\Omega |\mathbf{v}|^2\, d\mathbf{x} = \Big(-\frac{2}{R} - \lambda\Big)\int_\Omega |\nabla \mathbf{v}|^2\, d\mathbf{x}. \tag{32}$$

If $\lambda < 0$ and $R > -2/\lambda$, then the kinetic energy of the perturbation grows with a positive rate

$$r = -\frac{2}{R} - \lambda. \tag{33}$$

As R increases further, the growth rate r tends to $-\lambda$.

We can relate (32) to a more familiar expression for energy growth as follows. First, define the kinetic energy $k(t) = \int_\Omega |\mathbf{v}(\mathbf{x}, t)|^2\, d\mathbf{x}$. Second, divide (32) by $k(t)$ to get

$$\frac{d}{dt}(\log k)(0) = \frac{k'(0)}{k(0)} = r\,\frac{\int_\Omega |\nabla \mathbf{v}(\mathbf{x}, 0)|^2\, d\mathbf{x}}{\int_\Omega |\mathbf{v}(\mathbf{x}, 0)|^2\, d\mathbf{x}} \geq \frac{r}{c_P}, \tag{34}$$

where c_P is the constant in the Poincaré inequality (16). Thus kinetic energy k grows at least as fast as an exponential with exponent r/c_P, at least initially.

For $R = -2/\lambda$, the rate $r = 0$. Thus the instability is likely hard to see until R is substantially larger.

5.5 Spaces of perturbations

Suppose that the eigenproblem (21) has several negative eigenvalues

$$\lambda_1 \leq \lambda_2 \leq \cdots \lambda_k < 0 \tag{35}$$

with corresponding eigenfunctions $\mathbf{v}_i$. Then any combination of the $\mathbf{v}_i$'s can lead to a growing perturbation, as follows.

The eigenvalue problem may be written as

$$a(\mathbf{v}_i, \mathbf{w}) = \lambda_i^{-1} \mathcal{B}_{\mathbf{u}}(\mathbf{v}_i, \mathbf{w}) \quad \forall \mathbf{w} \in V,$$

where V is the subset of $H^1(\Omega)^d$ consisting of divergence-free functions vanishing on the boundary, defined in (12). The eigenvectors can be chosen to be orthogonal in the sense that

$$a(\mathbf{v}_i, \mathbf{v}_j) = 0 = \mathcal{B}_{\mathbf{u}}(\mathbf{v}_i, \mathbf{v}_j) \quad \forall i \neq j.$$

For suppose that $\lambda_i \neq \lambda_j$. Then

$$a(\mathbf{v}_i, \mathbf{v}_j) = \lambda_i^{-1} \mathcal{B}_{\mathbf{u}}(\mathbf{v}_i, \mathbf{v}_j)$$

but also

$$a(\mathbf{v}_i, \mathbf{v}_j) = \lambda_j^{-1} \mathcal{B}_{\mathbf{u}}(\mathbf{v}_i, \mathbf{v}_j)$$

using the symmetry of the bilinear forms. This cannot happen unless the forms are zero. For the case of a subspace of eigenvectors for a single eigenvalue, we can orthogonalize them with respect to the $a(\cdot, \cdot)$ bilinear form. But then

$$\mathcal{B}_{\mathbf{u}}(\mathbf{v}_i, \mathbf{v}_j) = \lambda_j a(\mathbf{v}_i, \mathbf{v}_j) = 0$$

as well. This establishes the orthogonalities.

Suppose that we have a mode comprised of several of the unstable modes:

$$\mathbf{v} = \sum_{i=1}^{k} c_j \mathbf{v}_j.$$

Then

$$\frac{-\mathcal{B}_{\mathbf{u}}(\mathbf{v}, \mathbf{v})}{a(\mathbf{v}, \mathbf{v})} = \frac{\sum_{j=1}^{k} c_j^2 (-\lambda_j) a(\mathbf{v}_j, \mathbf{v}_j)}{\sum_{j=1}^{k} c_j^2 a(\mathbf{v}_j, \mathbf{v}_j)} \geq -\lambda_k. \tag{36}$$

Thus

$$a(\mathbf{v}, \mathbf{v}) \leq \lambda_k^{-1} \mathcal{B}_{\mathbf{u}}(\mathbf{v}, \mathbf{v}),$$

and the conditions for energy instability at the beginning of Section 4 are satisfied if $R > 2/(-\lambda_k)$. Thus for sufficiently large R, the entire span of $\mathbf{v}_1, \ldots, \mathbf{v}_k$ can lead to instability.

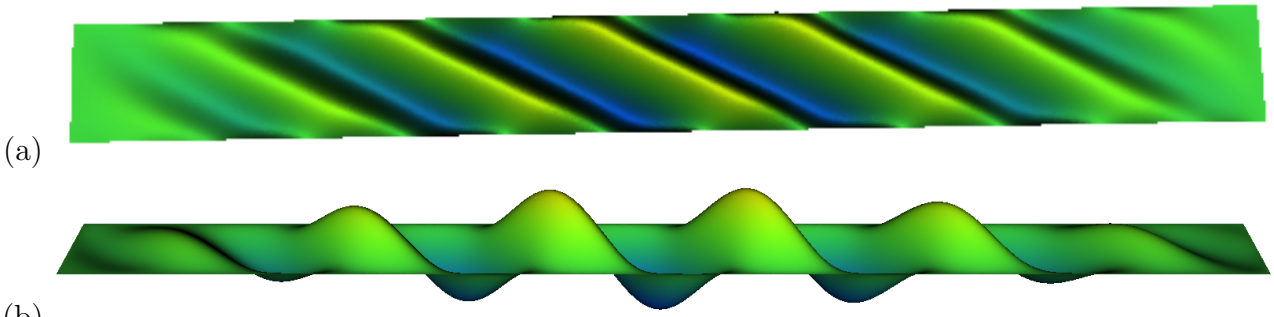

Figure 4: Flow components of the most unstable mode for Couette flow, computed on the domain (2) with meshsize parameter $M = 256$ and 200 iterations of the power method with $\mu = 0.01$: $L = 5$, $\lambda = -0.01122$. The meshsize parameter M is explained in section 8.7. Initial eigenvector approximation was given by (42) with the default frequency $\omega = 3.77$. (a) Horizontal flow component; compare Figure 2. (b) Vertical (cross-channel) flow component.

6 Example: instability of Couette flow

The definition for the Reynolds number R_0 given in [26] is

$$R_0 = U_0 h/\nu,$$

where ν is the kinematic viscosity, the flow rate at the top and bottom of the channel is $\pm U_0$, and $2h$ is the width of the channel. This is also the definition of Reynolds number used in [40]. We have chosen a different definition of Reynolds number based on the width of the channel as the length scale and the maximum flow rate minus the minimum flow rate as the velocity scale. Since Couette flow is linear in y, we have $\frac{\partial u}{\partial y} = U_0/h$. If we take for simplicity $U_0 = h$, we get $\frac{\partial u}{\partial y} = 1$.

In our computations, we took $h = \frac{1}{2}$ and $U_0 = \frac{1}{2}$, so we find that $R_0 = 1/4\nu = R/4$ in our notation. By numerical simulation, the authors of [26] found instability for $R_0 \approx 400$, or $R \approx 1600$ in our notation. Also see [25]. Similarly, a growing disturbance was observed in [40] for $R_0 \approx 360 \pm 10$. On the other hand, we identified an instability for $R >> 178$, as follows.

For Couette flow,

$$\nabla \mathbf{u} = \begin{pmatrix} 0 & 1 & 0 \\ 0 & 0 & 0 \\ 0 & 0 & 0 \end{pmatrix}.$$

(This nonnormal matrix arises in the linear stability analysis of Couette flow [17, 42].) Thus the variational form $\mathcal{B}_{\mathbf{u}}(\mathbf{v}, \mathbf{w})$ introduced in (14) takes the form

$$\mathcal{B}_{\mathbf{u}}(\mathbf{v}, \mathbf{w}) = \int_\Omega v_x w_y + v_y w_x \, d\mathbf{x}. \tag{37}$$

6.1 Couette eigenvalue bounds

In the material so far, we were agnostic about the choice of dimension d. Now we will restrict temporarily to the case $d = 2$. Our computations were carried out on a domain $\Omega \subset \mathbb{R}^2$ defined by (2). We can be a bit more precise than the general estimate (18). To begin with,

$$\left|\mathcal{B}_{\mathbf{u}}(\mathbf{v}, \mathbf{v})\right| = 2\left| \int_\Omega v_x v_y \, d\mathbf{x} \right| \leq \int_\Omega v_x^2 + v_y^2 \, d\mathbf{x}. \tag{38}$$

The Poincaré inequality in one dimension reads

$$\int_0^1 v(y)^2 \, dy \leq c_o \int_0^1 v'(y)^2 \, dy. \tag{39}$$

The best constant c_o is also defined by an eigenvalue problem, and in this case there is an explicit solution:

$$c_o = \frac{\int_0^1 v(y)^2 \, dy}{\int_0^1 v'(y)^2 \, dy}, \quad v(y) = \sin \pi y.$$

That is,

$$c_o = \frac{\int_0^1 \sin^2 \pi y \, dy}{\pi^2 \int_0^1 \cos^2 \pi y \, dy} = \frac{1}{\pi^2}.$$

Integrating (39) in x, we conclude that for any scalar function v

$$\int_\Omega v^2 \, d\mathbf{x} \leq \frac{1}{\pi^2} \int_\Omega (v_y)^2 \, d\mathbf{x} \leq \frac{1}{\pi^2} \int_\Omega |\nabla v|^2 \, d\mathbf{x}.$$

Applying this for each component of a vector function $\mathbf{v}$ we find

$$\int_\Omega v_x^2 + v_y^2 \, d\mathbf{x} \leq \frac{1}{\pi^2} \int_\Omega (v_{x,y})^2 + (v_{y,y})^2 \, d\mathbf{x} \leq \frac{1}{\pi^2} \int_\Omega |\nabla \mathbf{v}|^2 \, d\mathbf{x}.$$

Applying (38), we find

$$\left|\mathcal{B}_{\mathbf{u}}(\mathbf{v}, \mathbf{v})\right| \leq \frac{1}{\pi^2} a(\mathbf{v}, \mathbf{v}). \tag{40}$$

Thus the eigenvalues λ for the Couette problem satisfy

$$|\lambda| \leq \frac{1}{\pi^2}.$$

6.2 Couette eigenvalue computations

The Stokes-like system (30) was solved on the domain (2) using the iterated-penalty method [36] with the penalty parameter $r = 10^{-4}$. Typically, only 3 penalty iterations were needed to reduce the divergence of the numerical solution to the order of 10^{-12}.

L	start vector	λ	iterations	humps	R	M
5	$\mathbf{v} \equiv (0,1)$	-0.011221	698	6	178.2	128
5	$\mathbf{v}$ in (42)	-0.011221	100	6	178.2	128
5	$\mathbf{v}$ in (42)	-0.011222	200	6	178.2	256
7.5	$\mathbf{v}$ in (42)	-0.011257	200	9	177.1	256
10	$\mathbf{v}$ in (42)	-0.011268	200	12	177.5	128
10	$\mathbf{v}$ in (42)	-0.011269	300	12	177.5	256
20	$\mathbf{v}$ in (42)	-0.011279	200	23	177.3	128
20	$\mathbf{v}$ in (42)	-0.011280	300	23	177.3	256
40	$\mathbf{v}$ in (42)	-0.011283	300	47	177.3	512

Table 1: Dependence on channel length parameter L of stability limits λ. The "start vector" refers to the initial eigenvector approximation. The iterations column lists the number of power-method iterations used. In the first row, it was the number of iterations required to reduce the change in λ to less than 10^{-8}. The number H of "humps" is a guesstimate of the number of periods in the domain, with $2L/H$ being an estimate of the period length. $R = 2/\lambda$. The meshsize parameter M is explained in section 8.7. For start vectors in (42), the default frequency $\omega = 3.77$ was used. The shift $\mu = 0.01$ in all cases.

Functions $\mathbf{v} \in V^2$ are of the form $\mathbf{v} = (\psi_{,y}, -\psi_{,x})$ for suitable ψ. For such functions,

$$\mathcal{B}_{\mathbf{u}}(\mathbf{v}, \mathbf{v}) = -2 \int_\Omega \psi_{,x}\psi_{,y}\, d\mathbf{x}. \tag{41}$$

If $\psi(x, y) = f(x + y)$, then $\mathbf{v}(x, y) = (f'(x + y), -f'(x + y))$ and

$$\mathcal{B}_{\mathbf{u}}(\mathbf{v}, \mathbf{v}) = -2 \int_\Omega \big(f'\big)^2\, d\mathbf{x}.$$

Functions of this type thus give the maximal contribution to the perturbation form, without extraneous cancellations. This is consistent with what we see in Figure 2: the most unstable mode $\mathbf{v}$ appears to be a function of $x + y$ with a definite wave frequency of about 6/5. The meshsize parameter M is explained in section 8.7.

Of course, the actual modes must satisfy boundary conditions which are not consistent with this simple form, and so they are more complicated and must be computed numerically. But we can now try an initial eigenvector approximation of the form

$$\mathbf{v} = (1, -1) \sin\big(\omega(x + y)\big), \quad \omega = \frac{6\pi}{5} \approx 3.77 \text{ (default)}. \tag{42}$$

Using this starting vector, convergence is much faster, as indicated in Table 1.

For all domain length parameters L indicated in Table 1, an oscillatory, nearly periodic behavior was seen, with a definite wave frequency of about 6/5. The wave pattern is modulated by a function that goes to zero at the ends of the channel, being fairly constant in the middle, as shown for $L = 20$ in Figure 5.

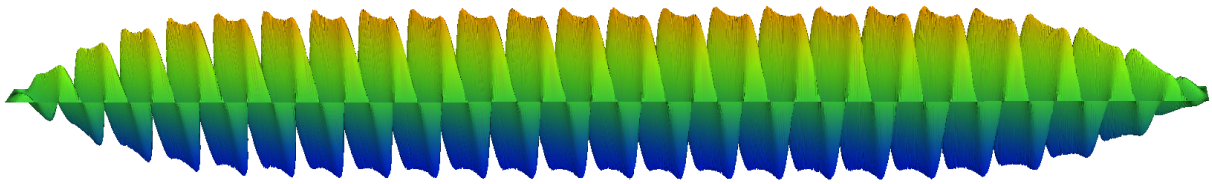

Figure 5: Horizontal flow component of the most unstable mode for Couette flow, computed on the domain (2) with meshsize parameter $M = 128$ and 200 iterations of the power method with $\mu = 0.01$: $L = 20$, $\lambda = -0.011279$. The meshsize parameter M is explained in section 8.7. Initial eigenvector approximation was given by (42).

The fact that the period is essentially the same for all values of L is consistent with the fact that the eigenvalues for $L = 10, 20, 40$ do not differ by much, as summarized in Table 1.

Better eigensolvers may be needed to resolve the modes accurately. On the other hand, the computed eigenvalues are much less dependent on the number of iterations, since the eigenvalue error is quadratic in the eigenvector error [5].

Table 1 summarizes the dependence of λ on L. This leads us to conjecture that λ_L tends to a limit λ_∞ as $L \to \infty$, where $2L$ is the channel length.

The results here are consistent with those of [26] who found *an* unstable mode for $R \approx 1600$, whereas we identified the most unstable mode for $R > 178$, or $R_0 > 45$. On the other hand, the results of Section 5.4 indicate that the growth rate will not be very big until R is much larger.

6.3 Couette flow symmetry

We can define a symmetry operator S as follows. Let us temporarily change coordinates so that the domain Ω in (2) is given by

$$\Omega = \left\{(x, y) \ : \ |x_1| \le L, \ |x_2| \le \tfrac{1}{2}\right\}. \tag{43}$$

For any scalar-valued function f, we define

$$Sf(\mathbf{x}) = -f(x_1, -x_2).$$

For a vector-valued function $\mathbf{v} = (v_1, v_2)$, we define something more complicated:

$$\mathbf{Sv}(\mathbf{x}) = (-v_1(x_1, -x_2), v_2(x_1, -x_2)).$$

Then the boundary-condition function $\mathbf{g}$ for Couette flow defined in (3) satisfies

$$\mathbf{Sg} = \mathbf{g}. \tag{44}$$

This is because $\mathbf{g}(\mathbf{x}) = (x_2, 0)$, and so

$$\mathbf{Sg}(\mathbf{x}) = (-(-x_2), 0) = \mathbf{g}(\mathbf{x}).$$

One way to think of $\mathbf{S}$ is to imagine its effect on a three-dimensional contour plot of the horizontal flow component v_1, as we have plotted frequently. Note that

$$(\mathbf{Sv})_1 = Sv_1,$$

although $(\mathbf{Sv})_2 \neq Sv_2$. A three-dimensional contour plot of a function f of two variables does two things: it represents the value of f by a color scale, but it also depicts the graph of f in three dimensions. Thus you see the value-colors placed on the graph at the appropriate height. If you turn a three-dimensional contour plot upside down, as is done in Figure 13, by rotating around the x_1 axis, then the color scale gets inverted as well as the ordering of x_2. This is precisely what S does.

Although the unperturbed solution $\mathbf{u} = \mathbf{g}$ for Couette flow is invariant under the action of $\mathbf{S}$, the perturbations are not. In particular, the operator $\mathbf{S}$ switches signs of eigenvalues. More precisely,

$$\begin{aligned} a(\mathbf{Sv}, \mathbf{Sv}) &= \int_\Omega |-v_{1,1}(x_1, -x_2)|^2 + |-(-v_{1,2}(x_1, -x_2))|^2 + \\ &\quad + |v_{2,1}(x_1, -x_2)|^2 + |-v_{2,2}(x_1, -x_2)|^2 \, d\mathbf{x} = a(\mathbf{v}, \mathbf{v}) \quad \forall\, \mathbf{v} \in H^1(\Omega)^d, \qquad (45) \\ \mathcal{B}_{\mathbf{u}}(\mathbf{Sv}, \mathbf{Sv}) &= 2\int_\Omega -v_1(x_1, -x_2)v_2(x_1, -x_2)\, d\mathbf{x} = -\mathcal{B}_{\mathbf{u}}(\mathbf{v}, \mathbf{v}) \quad \forall\, \mathbf{v} \in H^1(\Omega)^d, \end{aligned}$$

for $\mathbf{u} = \mathbf{g}$. Thus if $\mathbf{v}$ minimizes

$$\frac{\mathcal{B}_{\mathbf{u}}(\mathbf{v}, \mathbf{v})}{a(\mathbf{v}, \mathbf{v})}, \qquad (46)$$

with minimum value $-\lambda$, then $\mathbf{Sv}$ maximizes (46), with maximum value λ. This is confirmed in Figure 3. Note that (44) and (45) imply that $\mathcal{B}_{\mathbf{u}}(\mathbf{g}, \mathbf{g}) = 0$.

7 Time-dependent simulations

Since we have predicted time-dependent instabilities, it is natural to consider what they look like in practice. We know that the kinetic energy norm $\|\mathbf{u} - \mathbf{w}\|_{L^2(\Omega)}$ must increase initially as a function of time, but we were also curious about the strain energy norm. Thus we chose to measure $\|\nabla\mathbf{u} - \nabla\mathbf{w}\|_{L^2(\Omega)}$ as a function of time. Due to the Poincaré inequality, the kinetic energy is bounded by a constant times the strain energy. We return to examination of the kinetic energy in section 8.8.

In Figure 6(a), we see the results of simulations starting with a perturbation determined via 600 iterations of the power method, for two different Reynolds numbers, $R = 10$ and $R = 100$. The time-stepping scheme for solving (1) used throughout this section is the IMEX scheme described in section 8.2, together with the iterated-penalty method in section 8.3. Plotted is $\|\nabla\mathbf{u} - \nabla\mathbf{w}\|_{L^2(\Omega)}$ as a function of time, for $R = 10$ and $R = 100$. The steeper curve corresponds to $R = 10$. For reference, if we think of $\mathbf{u}$ as the unperturbed Couette flow, then

$$\|\nabla\mathbf{u}\|_{L^2(\Omega)} = \|\nabla\mathbf{g}\|_{L^2(\Omega)} = \sqrt{2L}$$

R	200	300	600	1600
$T_{\max}$	0.52	0.71	0.89	1.01

Table 2: Time $T_{\max}$ of maximal perturbation as a function of Reynolds number R. Based on the computations as in Figure 6. These times depend on the size of the initial perturbations.

$\|\mathbf{v}(t=0)\|_{H^1}$	2.104e-07	2.105e-05	2.105e-03	0.2110	2.110	21.10
$T_{\max}$	0.955	0.955	0.955	0.892	0.860	0.481
$\|\mathbf{v}(T_{\max})\|_{H^1}$	2.814e-07	2.815e-05	2.815e-03	0.2825	2.794	24.59

Table 3: Time $T_{\max}$ of maximal perturbation as a function of initial amplitude for Reynolds number $R = 600$. Based on the computations as in Figure 9(a).

for all t. Thus the largest perturbation for $R = 10$ is about the same size as the unperturbed Couette flow solution $\mathbf{u}$.

Both of these R values are below the expected threshold for instability, so it is not surprising to see that the norm $\|\nabla\mathbf{u} - \nabla\mathbf{w}\|_{L^2(\Omega)}$ decreases with time. We picked a larger perturbation at $t = 0$ for $R = 10$, and even though the initial perturbation is bigger than 1 in norm, the solution nevertheless returns to Couette flow exponentially in time. For the larger Reynolds number ($R = 100$), the behavior is more complex, with a much slower (and more complex) decay rate. Nevertheless, the perturbation eventually decays at a substantial rate.

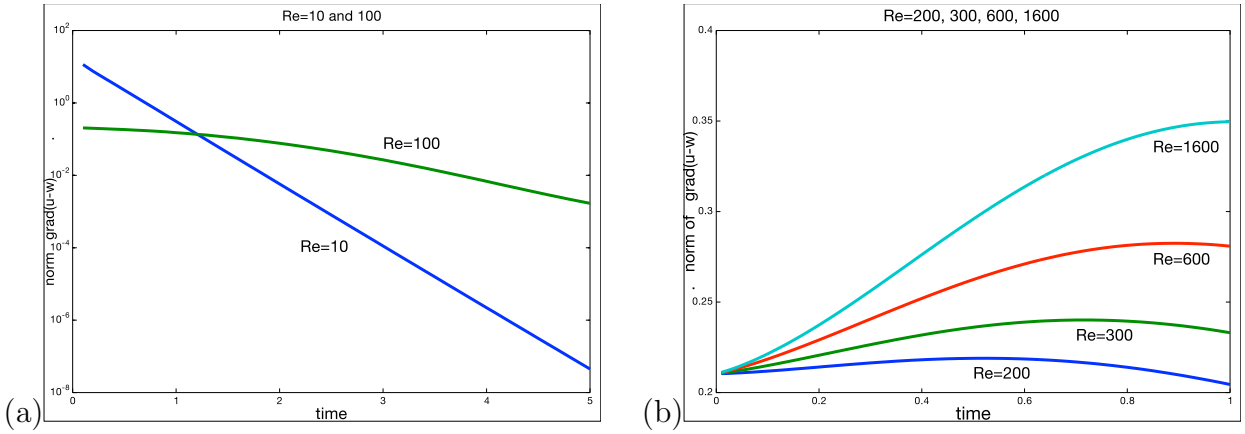

Figure 6: Behavior of the perturbation of the solution of the time-dependent Navier-Stokes equations on the domain (2) with $L = 5$ and meshsize parameter $M = 50$. The meshsize parameter M is explained in section 8.7. The initial perturbation was computed using 600 iterations with the initial eigenvector approximation $(0, 1)$. Shown are variation in time of the norm $\|\nabla\mathbf{u} - \nabla\mathbf{w}\|_{L^2(\Omega)}$ (a) for $R = 10$ and $R = 100$, and (b) for $R = 200$, $R = 300$, $R = 600$, and $R = 1600$.

In Figure 6(b), we see the results of simulations starting with a perturbation determined via 600 iterations of the power method, for four different Reynolds numbers, $R = 200$,

$R = 300$, $R = 600$, and $R = 1600$, up to time $T = 1$. Now we see that the perturbations grow initially, as expected. For $R = 200$, $R = 300$, and $R = 600$, the perturbations saturate before $T = 1$, and the difference $\|\nabla \mathbf{u} - \nabla \mathbf{w}\|_{L^2(\Omega)}$ starts decreasing. The times at which the perturbations are a maximum are given in Table 2.

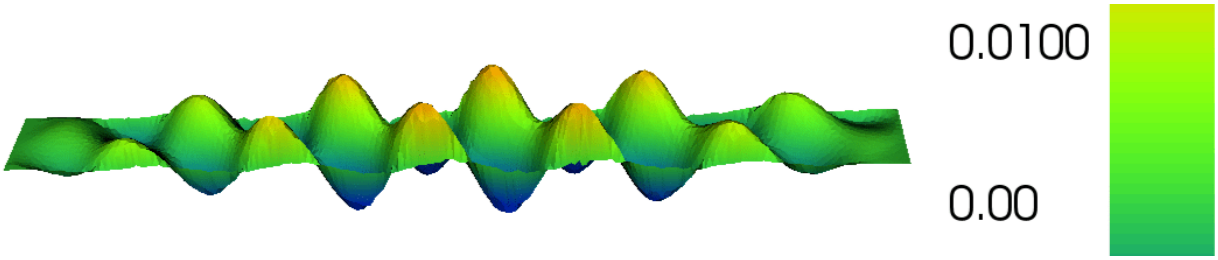

Figure 7: State of the perturbation $\mathbf{v}$ at $T = 0.5$, for $R = 200$. Determined by solving the time-dependent Navier-Stokes equations on the domain (2) with $L = 5$, where the initial perturbation was computed using 600 iterations with the initial eigenvector approximation $(0, 1)$ and meshsize parameter $M = 100$. The meshsize parameter M is explained in section 8.7.

7.1 Mode mutation

It is of interest to know what happens when the perturbations reach their maximal size. In Figure 7 we see the horizontal flow component of the perturbation $\mathbf{v} = \mathbf{u} - \mathbf{w}$ at $T = 0.5$, for $R = 200$ and $L = 5$. This should be compared to the initial perturbation shown in Figure 2. For $R = 200$, $T = 0.5$ is close to the time when the maximum of $\|\nabla \mathbf{v}\|_{L^2(\Omega)}$ occurs, as indicated in Figure 6(b). We see that the perturbation has become significantly modified, and presumably this different profile leads to the dissipation of the unstable mode. In particular, the initial most-unstable mode is converted into a higher-frequency mode, that then dissipates to zero, as indicated in Figure 8(a). For $5 < t < 7$, $\|\nabla \mathbf{v}\|_{L^2(\Omega)}$ appears asymptotic to $0.6e^{-(5/6)t}$, as indicated by the thin straight line in Figure 8(a).

Figure 8(b), we see the results of simulations starting with a perturbation determined for three different Reynolds numbers, $R = 600$, $R = 2000$, and $R = 4000$, up to time $T = 1$. These calculations were done with a coarser mesh parameter $M = 25$ and only 400 iterations of the power method to expedite the computations. This provides a resolution test via the case $R = 600$. We see there are small differences from the case $M = 50$ shown in Figure 6(b), but the general character is preserved. This gives us confidence in the general form for $R = 2000$ and $R = 4000$.

7.2 Amplitude dependence

In Figure 9(a), we see the results of simulations starting with different perturbations for Reynolds number $R = 600$, up to time $T = 1$. The times at which the perturbations are a maximum are given in Table 3. For the smallest amplitudes, the maximum occurs at the same time, but the time at which the maximum occurs decreases as the amplitude increases.

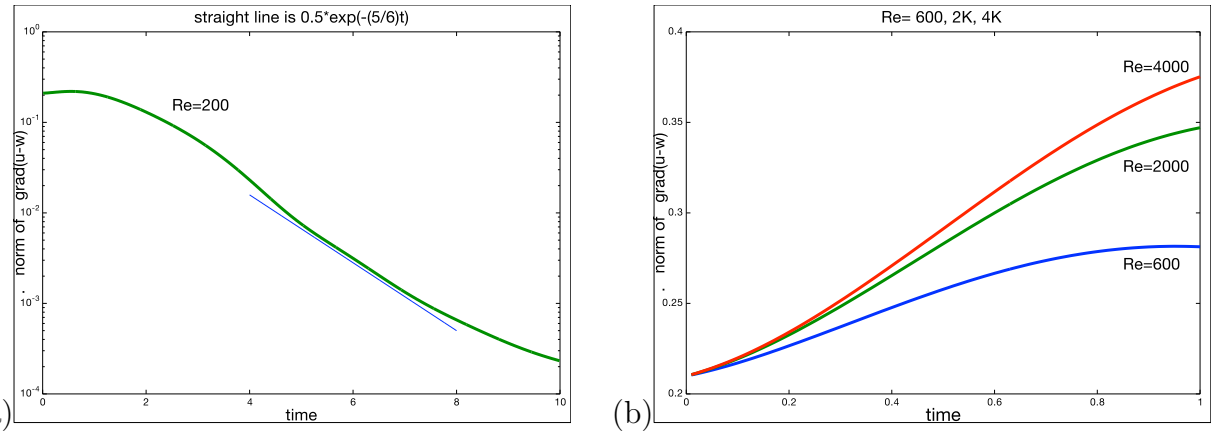

(a) (b)

Figure 8: (a) Ultimate fate of the perturbation for $R = 200$. Determined by solving the time-dependent Navier-Stokes equations on the domain (2) with $L = 5$, where the initial perturbation was computed using 600 iterations with the initial eigenvector approximation $(0, 1)$ and meshsize parameter 100.
(b) Behavior of the perturbation of the solution of the time-dependent Navier-Stokes equations on the domain (2) with $L = 5$ and meshsize parameter 25. The initial perturbation was computed using 400 iterations with the initial eigenvector approximation $(0, 1)$. Shown are variation in time of the norm $\|\nabla \mathbf{u} - \nabla \mathbf{w}\|_{L^2(\Omega)}$ for $R = 600$, $R = 2000$, and $R = 4000$.

Thus lowering the amplitude tends to flatten the curve. The larger amplitudes peak earlier and also do not reach as high in terms of a factor times the initial perturbation.

We have seen substantial variations in the perturbations as a function of Reynolds number. Noteworthy is that fact that the rate of growth of the perturbations is much larger than predicted in Section 5.4. Moreover, the growth rate increases as R increases. However, the dependence on initial perturbation amplitude is quite different.

Since the nonlinearity of the Navier-Stokes equations is substantial for $R = 600$, we might expect that there would be a strong dependence of, say, the solution at $T = 1$ on the initial amplitude. However, the dependence in terms of flow profile appears to be minimal. In Figure 9(a), we see the results of simulations with $R = 600$ for various initial amplitudes a for the perturbation. These represent computations of

$$f_a(t) := \|\nabla \mathbf{u}^a(t) - \nabla \mathbf{w}^a(t)\|_{L^2(\Omega)} \tag{47}$$

as a function of t, where

$$\nabla \mathbf{u}^a(0) - \nabla \mathbf{w}^a(0) = a\phi \tag{48}$$

and ϕ is the most unstable mode computed as in Section 6.2. Only for the largest initial perturbation does the solution differ in character from the smaller amplitudes. In particular, it reaches saturation, and then starts to decay, at a smaller time than the generic case. For the largest amplitude, the initial "perturbation" is larger than the base flow size by a substantial margin.

For the smaller amplitudes, the profiles $f_a(t)$ defined in (47) satisfy $f_a/f_b = c_{a,b}$ for an appropriate constant $c_{a,b}$, to several significant digits (greater than graphical accuracy). This

is as if the effect of the perturbation were linear, which it appears nearly to be for a not too big.

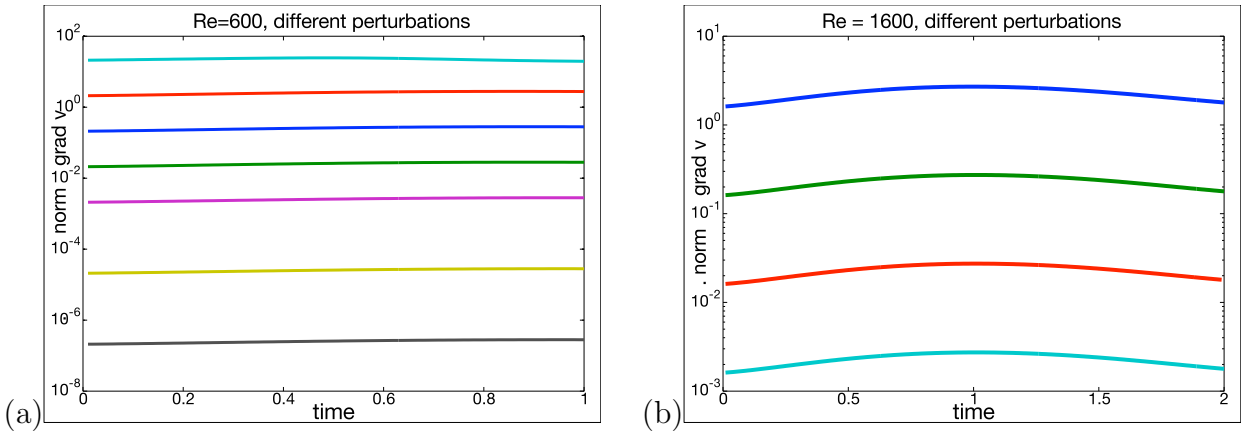

Figure 9: Behavior of the perturbation (47) of the solution of the time-dependent Navier-Stokes equations on the domain (2) with $L = 5$. Shown are variation in time of the norm $\|\nabla \mathbf{u} - \nabla \mathbf{w}\|_{L^2(\Omega)}$. (a) $R = 600$. The initial perturbation ϕ was computed using 600 iterations with the initial eigenvector approximation $(0, 1)$. For larger amplitudes $a = 1000, 100, 10, 1$, meshsize parameter $M = 50$, and smaller amplitudes $a = 10^{-1}, 10^{-3}, 10^{-5}$, meshsize parameter $M = 25$. (b) $R = 1600$. The initial perturbation ϕ was computed using 100 iterations with the initial eigenvector approximation (42) using $\omega = 3.77$, with meshsize parameter $M = 100$.

7.3 Physical interpretation

We can relate the abstract results to physical experiments as follows. Most of our computations for the time-dependent problems were done in a channel with a 10 to 1 (length to width) aspect ratio. Thus imagine a channel 10 centimeters wide and 1 meter long. Then the Reynolds number R is

$$R = \frac{1000\, U}{\nu}$$

if the flow speed difference is U meters per second, and the kinematic viscosity is in centimeters-squared per second. With these units, the time units in the computations is seconds.

For simplicity, assume that the speed at the bottom is $-\frac{1}{2}U$ and the speed at the at the top is $+\frac{1}{2}U$. Let $\mathcal{T}$ be the time it takes for a fluid particle to go from one end of the channel to the other end (at the top or bottom), which is $2/U$ seconds, since U is measured in meters per second and the channel length is a meter. We could call $\mathcal{T} = 2/U$ the *exit time*:

$$\mathcal{T} = \frac{2000}{\nu R}. \tag{49}$$

Thus for $R = 2000$, the exit time $\mathcal{T}$ is $1/\nu$ seconds, again with ν given in centimeters-squared per second. For larger R, $\mathcal{T}$ is smaller, and for smaller R is is larger.

For air at -40 degrees Centigrade, $\nu = 0.1$ centimeters-squared per second, and for water at $+20$ degrees Centigrade, $\nu = 0.01$ centimeters-squared per second [21]. Thus for air at -40 degrees Centigrade and $R = 2000$, $\mathcal{T} = 10$ seconds; for water at $+20$ degrees Centigrade and $R = 2000$, $\mathcal{T} = 100$ seconds. For air at -40 degrees Centigrade and $R = 200$, $\mathcal{T} = 100$ seconds; for water at $+20$ degrees Centigrade and $R = 200$, $\mathcal{T} = 1000$ seconds. Therefore our calculations for $R = 200$ indicate that the perturbation will dissipate long before the exit time. These data and more are summarized in Table 4.

fluid	ν	temperature	$R = 20000$	$R = 2000$	$R = 200$
water	0.010	20 C = 68 F	$\mathcal{T} = 10$	$\mathcal{T} = 100$	$\mathcal{T} = 1000$
air	0.100	-40 C $=-40$ F	$\mathcal{T} = 1$	$\mathcal{T} = 10$	$\mathcal{T} = 100$
motor oil 10W	12.95	-17.78 C = 0 F	$\mathcal{T} = 0.008$	$\mathcal{T} = 0.077$	$\mathcal{T} = 0.772$

Table 4: Kinematic viscosity coefficients ν and exit times $\mathcal{T}$ defined in (49) for various fluids [21] at various Reynolds numbers R. The units for ν are cm^2/second and the unit for $\mathcal{T}$ is seconds.

It may seem odd that a higher viscosity leads to a shorter exit time. What this means is as follows. For a larger viscosity, you have to have a larger velocity U to get the same Reynolds number R. For example, for motor oil (10W, at zero degrees F), to achieve $R = 200$ you need to pump our channel at a speed $U = 2.59$ meters per second. At slower speeds, the flow will be stable, as indicated in Figure 6. For less viscous fluids, instabilities arise at more modest pumping rates. Thus for the same speeds, less viscous fluids are more unstable, as we expect. This makes it easier to study instabilities in water than in air.

It may seem surprising that air appears to be more viscous than water. This is a result of the fact that the kinematic viscosity is defined by dividing the (dynamic or absolute) viscosity by the density, and water is about one thousand times denser than air. The absolute viscosity of air and water differ by a factor of about 100 in the opposite ratio. However, the ratio is very dependent on temperature. The viscosity of air increases with temperature, whereas water viscosity decreases as a function of temperature.

8 Time-dependent computational details

The implicit Euler method for solving the equations (1), or (4), can be written in variational form as follows: find $\hat{\mathbf{u}}^n \in V + \mathbf{g}$ such that

$$\frac{R}{\Delta t}(\hat{\mathbf{u}}^n - \hat{\mathbf{u}}^{n-1}, \mathbf{v}) + a(\hat{\mathbf{u}}^n, \mathbf{v}) + R\, c(\hat{\mathbf{u}}^n, \hat{\mathbf{u}}^n, \mathbf{v}) = 0 \quad \forall \mathbf{v} \in V, \tag{50}$$

where $\mathbf{g} = (2y - 1, 0)$ for the Couette problem. Thus we can write $\hat{\mathbf{u}}^n = \mathbf{u}^n + \mathbf{g}$ for $\mathbf{u}^n \in V$, simplifying to

$$\frac{R}{\Delta t}(\mathbf{u}^n - \mathbf{u}^{n-1}, \mathbf{v}) + \big(a(\mathbf{u}^n, \mathbf{v}) + a(\mathbf{g}, \mathbf{v})\big) + R\, c(\mathbf{u}^n + \mathbf{g}, \mathbf{u}^n + \mathbf{g}, \mathbf{v}) = 0 \quad \forall \mathbf{v} \in V.$$

The nonlinear term simplifies via

$$\begin{aligned} c(\mathbf{u}^n+\mathbf{g},\mathbf{u}^n+\mathbf{g},\mathbf{v}) &= c(\mathbf{u}^n,\mathbf{u}^n+\mathbf{g},\mathbf{v}) + c(\mathbf{g},\mathbf{u}^n+\mathbf{g},\mathbf{v}) \\ &= c(\mathbf{u}^n,\mathbf{u}^n,\mathbf{v}) + c(\mathbf{u}^n,\mathbf{g},\mathbf{v}) + c(\mathbf{g},\mathbf{u}^n,\mathbf{v}) + c(\mathbf{g},\mathbf{g},\mathbf{v}). \end{aligned} \tag{51}$$

But $\mathbf{g}\cdot\nabla\mathbf{g} = (2y-1)g_{x,x} = 0$, so $c(\mathbf{g},\mathbf{g},\mathbf{v}) = 0$ for all $\mathbf{v}$. Define a symmetrized nonlinear form via

$$\hat{c}(\mathbf{u},\mathbf{w},\mathbf{v}) = c(\mathbf{u},\mathbf{w},\mathbf{v}) + c(\mathbf{w},\mathbf{u},\mathbf{v}). \tag{52}$$

Thus $\mathbf{u}^n \in V$ is defined by solving

$$\frac{R}{\Delta t}(\mathbf{u}^n,\mathbf{v}) + a(\mathbf{u}^n,\mathbf{v}) + R\big(c(\mathbf{u}^n,\mathbf{u}^n,\mathbf{v}) + \hat{c}(\mathbf{u}^n,\mathbf{g},\mathbf{v})\big) = \frac{R}{\Delta t}(\mathbf{u}^{n-1},\mathbf{v}) - a(\mathbf{g},\mathbf{v}) \tag{53}$$

for all $\mathbf{v} \in V$. Notice that the base solution, which we have referred to here as $\hat{\mathbf{u}}$, satisfies $\hat{\mathbf{u}} = \mathbf{g}$ for all t if there is no perturbation at $t = 0$. So $\mathbf{u} = \hat{\mathbf{u}} - \mathbf{g}$ corresponds directly to (minus) the perturbation $\mathbf{v}$ that we are interested in studying, even though we are computing it as a solution of Navier-Stokes, as opposed to using the equation (7) which also defines $\mathbf{v}$. Thus the formulation (58) gives us a direct way to assess the perturbation $\mathbf{v} = \mathbf{u} - \mathbf{w}$ described in Section 2.

8.1 Basic stability

The basic Euler method (53) enjoys some numerical stability properties, as follows. Choose $\mathbf{v} = \mathbf{u}^n$ in (53) and use (9) to get

$$\frac{R}{\Delta t}\|\mathbf{u}^n\|^2_{L^2(\Omega)} + \|\nabla\mathbf{u}^n\|^2_{L^2(\Omega)} + Rc(\mathbf{u}^n,\mathbf{g},\mathbf{u}^n) = \frac{R}{\Delta t}(\mathbf{u}^{n-1},\mathbf{u}^n) - a(\mathbf{g},\mathbf{u}^n). \tag{54}$$

But for any $\mathbf{v} \in V$, integration by parts shows that

$$a(\mathbf{g},\mathbf{v}) = \int_\Omega \nabla\mathbf{g} : \nabla\mathbf{v}\, d\mathbf{x} = \int_\Omega v_{x,y}\, d\mathbf{x} = 0,$$

due to the boundary conditions satisfied by $\mathbf{v}$. Thus (54) becomes

$$\begin{aligned} \frac{R}{\Delta t}\|\mathbf{u}^n\|^2_{L^2(\Omega)} + \|\nabla\mathbf{u}^n\|^2_{L^2(\Omega)} + R\,\mathcal{B}_{\mathbf{g}}(\mathbf{u}^n,\mathbf{u}^n) &= \frac{R}{\Delta t}(\mathbf{u}^{n-1},\mathbf{u}^n) \\ &= \frac{R}{\Delta t}\|\mathbf{u}^n\|^2_{L^2(\Omega)} - \frac{R}{\Delta t}(\delta\mathbf{u}^n,\mathbf{u}^n), \end{aligned} \tag{55}$$

where $\delta\mathbf{u}^n = \mathbf{u}^n - \mathbf{u}^{n-1}$. The standard stability estimate is obtained by applying the Cauchy-Schwarz inequality and the arithmetic-geometric mean inequality to the first line in (55) to yield

$$\frac{R}{2\Delta t}\|\mathbf{u}^n\|^2_{L^2(\Omega)} + \|\nabla\mathbf{u}^n\|^2_{L^2(\Omega)} + R\,\mathcal{B}_{\mathbf{u}}(\mathbf{u}^n,\mathbf{u}^n) \le \frac{R}{2\Delta t}\|\mathbf{u}^{n-1}\|^2_{L^2(\Omega)},$$

which means that $\|\mathbf{u}^n\|_{L^2(\Omega)} \le \|\mathbf{u}^{n-1}\|_{L^2(\Omega)}$ for R sufficiently small. But we can also use (55) to get

$$\frac{R}{\Delta t}(\delta\mathbf{u}^n,\mathbf{u}^n) + \|\nabla\mathbf{u}^n\|^2_{L^2(\Omega)} + R\,\mathcal{B}_{\mathbf{u}}(\mathbf{u}^n,\mathbf{u}^n) = 0. \tag{56}$$

Thus if $\mathbf{u}^n$ is close to the most unstable mode and R is sufficiently large, we must have $(\delta\mathbf{u}^n, \mathbf{u}^n) > 0$. Of course, all of this assumes that we have solved the nonlinear system (53) exactly.

8.2 The nonlinear system

Let us introduce some notation to simplify discussion and implementation. Define $\tau = R/\Delta t$ and

$$\tilde{a}(\mathbf{u}, \mathbf{v}) = \tau\,(\mathbf{u}, \mathbf{v}) + a(\mathbf{u}, \mathbf{v}), \qquad a_g(\mathbf{u}, \mathbf{v}) = \tilde{a}(\mathbf{u}, \mathbf{v}) + R\,\hat{c}(\mathbf{u}, \mathbf{g}, \mathbf{v}). \tag{57}$$

With this notation, (53) becomes

$$a_g(\mathbf{u}^n, \mathbf{v}) + R\,c(\mathbf{u}^n, \mathbf{u}^n, \mathbf{v}) = \tau\,(\mathbf{u}^{n-1}, \mathbf{v}) - a(\mathbf{g}, \mathbf{v}) \tag{58}$$

for all $\mathbf{v} \in V$.

There are many different strategies for solving (58) for $\mathbf{u}^n$. But the simplest is to evaluate the nonlinear term at the previous time step, yielding what is called an IMEX (linearly IMplicit–nonlinearly EXplicit) scheme [23]: find $\mathbf{u}^n \in V$ such that

$$a_g(\mathbf{u}^n, \mathbf{v}) = -R\,c(\mathbf{u}^{n-1}, \mathbf{u}^{n-1}, \mathbf{v}) + \tau\,(\mathbf{u}^{n-1}, \mathbf{v}) - a(\mathbf{g}, \mathbf{v}) \tag{59}$$

for all $\mathbf{v} \in V$. This can be simplified since

$$\begin{aligned} \hat{c}(\mathbf{u}, \mathbf{g}, \mathbf{v}) &= c(\mathbf{u}, \mathbf{g}, \mathbf{v}) + c(\mathbf{g}, \mathbf{u}, \mathbf{v}) = -c(\mathbf{u}, \mathbf{v}, \mathbf{g}) - c(\mathbf{g}, \mathbf{v}, \mathbf{u}) \\ &= -\int_\Omega \mathbf{g}^t\big(\nabla\mathbf{v} + \nabla\mathbf{v}^t\big)\mathbf{u}\,d\mathbf{x}, \end{aligned} \tag{60}$$

but in any case, this term makes the linear system to be solved in (59) nonsymmetric. On the other hand, we can show that this system is coercive, as follows.

We have

$$\begin{aligned} |\hat{c}(\mathbf{v}, \mathbf{g}, \mathbf{v})| &= \Big|\int_\Omega \mathbf{g}^t\big(\nabla\mathbf{v} + (\nabla\mathbf{v})^t\big)\mathbf{v}\,d\mathbf{x}\Big| \le 2\|\mathbf{g}\|_{L^\infty(\Omega)}\,(a\,(\mathbf{v}, \mathbf{v}))^{1/2}\,(\mathbf{v}, \mathbf{v})^{1/2} \\ &\le \frac{1}{2R}a\,(\mathbf{v}, \mathbf{v}) + 2R\|\mathbf{g}\|^2_{L^\infty(\Omega)}\,(\mathbf{v}, \mathbf{v})\,. \end{aligned} \tag{61}$$

Therefore (61) implies that

$$\begin{aligned} a_g(\mathbf{v}, \mathbf{v}) &= \tilde{a}(\mathbf{v}, \mathbf{v}) - R\int_\Omega \mathbf{g}^t\big(\nabla\mathbf{v} + (\nabla\mathbf{v})^t\big)\mathbf{v}\,d\mathbf{x} \\ &\ge \tfrac{1}{2}a(\mathbf{v}, \mathbf{v}) + \left(\tau - 2R^2\|\mathbf{g}\|^2_{L^\infty(\Omega)}\right)(\mathbf{v}, \mathbf{v}) \ge \tfrac{1}{2}\tilde{a}(\mathbf{v}, \mathbf{v}) \end{aligned} \tag{62}$$

for $\tau \ge 4R^2\|\mathbf{g}\|^2_{L^\infty(\Omega)}$. For Couette flow, $\|\mathbf{g}\|_{L^\infty(\Omega)} = \frac{1}{2}$, so this condition reduces to $\tau \ge R^2$, or $\Delta t \le 1/R$. In our computations in section 7, we chose $\Delta t = (10R)^{-1}$ to be conservative.

8.3 Iterated penalty method

Implementation of the IMEX scheme (59) also requires a strategy for staying in (or near) the divergence-free space V. We can write (59) as

$$\begin{aligned} \tilde{a}_R(\mathbf{u}^n, \mathbf{v}) &= F^n(\mathbf{v}) \quad \forall \mathbf{v} \in V, \\ F^n(\mathbf{v}) &= -R\, c(\mathbf{u}^{n-1},\mathbf{u}^{n-1}, \mathbf{v}) + \frac{R}{\Delta t}(\mathbf{u}^{n-1}, \mathbf{v}) - a(\mathbf{g}, \mathbf{v}), \end{aligned} \tag{63}$$

where

$$\tilde{a}_R(\mathbf{u}, \mathbf{v}) = \tilde{a}(\mathbf{u}, \mathbf{v}) - R \int_\Omega \mathbf{g}^t \big(\nabla \mathbf{v} + (\nabla \mathbf{v})^t\big)\mathbf{u}\, d\mathbf{x}.$$

Then the iterated penalty method for (63) takes the form

$$\begin{aligned} \tilde{a}_R(\tilde{\mathbf{u}}^\ell, \mathbf{v}) + \rho(\nabla\cdot \tilde{\mathbf{u}}^\ell, \nabla\cdot \mathbf{v}) &= F^n(\mathbf{v}) - (\nabla\cdot \mathbf{w}^\ell, \nabla\cdot \mathbf{v})\ \forall \mathbf{v} \in V, \\ \mathbf{w}^{\ell+1} &= \mathbf{w}^\ell + \rho\, \tilde{\mathbf{u}}^\ell, \end{aligned} \tag{64}$$

where we start with $\mathbf{w}^0 \equiv \mathbf{0}$. This is guaranteed [4] to converge since $\tilde{a}_R(\mathbf{u}, \mathbf{v})$ is coercive, in view of (62). Once this converges, we set $\mathbf{u}^n = \tilde{\mathbf{u}}^\ell$. If desired, we also have the pressure $p^n = -\nabla\cdot \mathbf{w}^\ell$. In most of our time-dependent computations, we chose $\rho = 10^5$.

8.4 Long-time simulations

Longer-time simulations are required to examine the fate of perturbations for larger Reynolds numbers. We can define the persistence time T_P for a perturbation by the inequality

$$\|\nabla \mathbf{v}(t)\|_{L^2(\Omega)} < \|\nabla \mathbf{v}(0)\|_{L^2(\Omega)} \quad \forall t > T_P. \tag{65}$$

Note that, as we have defined it, T_P is not necessarily the first time $t > 0$ that

$$\|\nabla \mathbf{v}(t)\|_{L^2(\Omega)} = \|\nabla \mathbf{v}(0)\|_{L^2(\Omega)}$$

for some $t > 0$. As we see in Figure 11, the norm $\|\nabla \mathbf{v}(t)\|_{L^2(\Omega)}$ is not monotonic in t for $t > T_{\max}$. We estimate persistence times for several values of R in Table 5.

To simulate longer evolution of perturbations, another approach is available. Instead of integrating (1) with an initial perturbation, we can instead directly integrate (7). Then the evolution equation for $\mathbf{v}$ is

$$\mathbf{v}_t - \frac{1}{R}\Delta \mathbf{v} + \mathbf{g}\cdot\nabla \mathbf{v} + \mathbf{v}\cdot\nabla \mathbf{g} - \mathbf{v}\cdot\nabla \mathbf{v} + \nabla \hat{o} = \mathbf{0} \text{ in } \Omega,$$

where $\hat{o}$ is a suitably scaled pressure. Note that we have simplified the equation by using the fact that the unperturbed solution $\mathbf{u} = \mathbf{g} = (2y - 1, 0)$ for the Couette problem for all time. The idea is that $\mathbf{v}$ will be small, so that we can approximate (7) with all advection terms handled explicitly. The corresponding implicit Euler method can be written in variational form as follows: find $\mathbf{v}^n \in V$ such that

$$(\mathbf{v}^{n+1}, \mathbf{z}) + \frac{1}{\tau} a(\mathbf{v}^{n+1}, \mathbf{z}) = (\mathbf{v}^n, \mathbf{z}) - \Delta t\, \hat{c}(\mathbf{v}^n, \mathbf{g}, \mathbf{z}) + \frac{1}{\tau}\, c(\mathbf{v}^n, \mathbf{v}^n, \mathbf{z}) \quad \forall \mathbf{z} \in V. \tag{66}$$

We can write (66) as

$$\begin{aligned} \tilde{a}(\mathbf{v}^{n+1},\mathbf{z}) &= F^n(\mathbf{z}) \quad \forall \mathbf{z}\in V_h, \\ F^n(\mathbf{z}) &= \tau\,(\mathbf{v}^n,\mathbf{z}) - R\,\hat{c}(\mathbf{v}^n,\mathbf{g},\mathbf{z}) + R\,c(\mathbf{v}^n,\mathbf{v}^n,\mathbf{z}). \end{aligned} \tag{67}$$

Then the iterated-penalty method for (67) takes the form

$$\begin{aligned} \tilde{a}(\tilde{\mathbf{v}}^\ell,\mathbf{z}) + \rho(\nabla\cdot\tilde{\mathbf{v}}^\ell,\nabla\cdot\mathbf{z}) &= F^n(\mathbf{z}) - (\nabla\cdot\boldsymbol{\omega}^\ell,\nabla\cdot\mathbf{z})\ \forall \mathbf{z}\in W_h, \\ \boldsymbol{\omega}^{\ell+1} &= \boldsymbol{\omega}^\ell + \rho\,\tilde{\mathbf{v}}^\ell, \end{aligned} \tag{68}$$

where we start with $\boldsymbol{\omega}^0 \equiv \mathbf{0}$. This is guaranteed [4] to converge since $\tilde{a}(\mathbf{u},\mathbf{z})$ is coercive. Once this converges, we set $\mathbf{v}^{n+1} = \tilde{\mathbf{v}}^\ell$. If desired, we also have the pressure $\hat{o}^{n+1} = -\nabla\cdot\boldsymbol{\omega}^\ell$.

In Figure 11(a), computations of the norm $\|\nabla\mathbf{v}\|_{L^2(\Omega}$ of the solution $\mathbf{v}$ of (7) are depicted for $R = 1600$, $R = 3000$, and $R = 10000$. These were done on the domain (2) with $L = 5$ and meshsize parameter $M = 50$, using the scheme (67), combined with the iterated-penalty method (68). The values of Δt used are indicated in Table 5. For reference, for the unperturbed solution $\mathbf{u}$, $\|\nabla\mathbf{u}\|_{L^2(\Omega} = \|\nabla\mathbf{g}\|_{L^2(\Omega} = \sqrt{2L}$.

The key to success of the new scheme was to take the penalty parameter ρ to scale with τ. Otherwise, the iterated-penalty method was slow to converge and the divergence of the solution was not small. Sometimes, this led to significant inaccuracies in the H^1 norm of $\mathbf{v}$, and ultimately to instability of the numerical solution (i.e., blow-up). In most of our time-dependent computations reported in this and subsequent sections, we picked $\rho = 10\tau$. This formula may make ρ too small for smaller R and larger Δt, but it was used successfully for the computations reported in Table 5.

We chose to stop at $R = 10^5$ since various changes occur for much larger Reynolds numbers. For example, the drag crisis [16] occurs for $R < 10^6$. This may be related to a change in boundary conditions due to the high flow rate such as slip ($\mathbf{u}\cdot\mathbf{n} = 0$) boundary conditions, with suitable friction coefficient [12]. However, our numerical methods were capable of computing for $R \geq 10^6$.

Another approach is just to solve (67) in W_h and then project $\mathbf{v}^{n+1}$ back to V_h via the Stokes projection. More precisely, we solve

$$\tilde{a}(\hat{\mathbf{v}}^{n+1},\mathbf{z}) = \tau\,(\mathbf{v}^n,\mathbf{z}) - R\,\hat{c}(\mathbf{v}^n,\mathbf{g},\mathbf{z}) + R\,c(\mathbf{v}^n,\mathbf{v}^n,\mathbf{z}) \quad \forall \mathbf{z}\in W_h. \tag{69}$$

Then we use the iterated-penalty method

$$\begin{aligned} a(\tilde{\mathbf{v}}^\ell,\mathbf{z}) + \rho(\nabla\cdot\tilde{\mathbf{v}}^\ell,\nabla\cdot\mathbf{z}) &= a(\hat{\mathbf{v}}^{n+1},\mathbf{z}) - (\nabla\cdot\boldsymbol{\omega}^\ell,\nabla\cdot\mathbf{z})\ \forall \mathbf{z}\in W_h, \\ \boldsymbol{\omega}^{\ell+1} &= \boldsymbol{\omega}^\ell + \rho\,\tilde{\mathbf{v}}^\ell, \end{aligned} \tag{70}$$

where we start with $\boldsymbol{\omega}^0 \equiv \mathbf{0}$. This is guaranteed [4] to converge since $a(\mathbf{u},\mathbf{z})$ is coercive. Once this converges, we set $\mathbf{v}^{n+1} = \tilde{\mathbf{v}}^\ell$. If desired, we also have the pressure $\hat{o}^{n+1} = -\nabla\cdot\boldsymbol{\omega}^\ell$. However, this was not more efficient than using (68) which converged quickly with the appropriate ρ values. On the other hand, for even larger Reynolds numbers, it may be necessary to use the modified approach.

8.5 Movie

In Figure 7, we presented the state of the perturbation for $R = 200$ at the time near where it is maximal. This gives a good indication of how the perturbation gets modified before it begins to dissipate. Here we extend this to a complete time series for $R = 1600$ out to time $T = 5$ where it is exponentially decreasing.

In Figure 10, we present a time series of the horizontal velocity of the perturbation $\mathbf{v}$ at different times for $R = 1600$. The scale in the figure changes after $T = 2.0$ as the perturbation dissipates. The figures were computed with algorithm (66) with $\Delta t = 0.001$.

We see how the perturbation transforms from the initial unstable mode into something where the waves run in the opposite direction, somewhat analogous to the most stable mode. However, its character is more complex in nature. The behavior of perturbations for larger Reynolds numbers is similar (data not shown).

As the perturbation evolves in time, the wavetrain transitions from an upper-left to lower-right orientation (at t=0) to an upper-right to lower-left orientation, which we begin to see for $t \geq 1$. For $t > 5$ this waveform elongates, and we can see in Figure 12 the result for $t = 10$ and $R = 10^5$.

8.6 Second-order time stepping

Although the scheme (66) has proved quite effective for Reynolds numbers up to 10^4, it becomes prohibitive for larger Re. Thus we developed a simple scheme that is second-order in time by a simple modification:

$$\frac{1}{\Delta t}(\mathbf{v}^{n+1} - \mathbf{v}^n, \mathbf{z}) + \frac{1}{2R}\big(a(\mathbf{v}^{n+1}, \mathbf{z}) + a(\mathbf{v}^n, \mathbf{z})\big) = -\hat{c}(E\mathbf{v}^n, \mathbf{g}, \mathbf{z}) + c(E\mathbf{v}^n, E\mathbf{v}^n, \mathbf{z}) \qquad (71)$$

for all $\mathbf{z} \in V$, where $E\mathbf{v}^n$ is obtained by extrapolation:

$$E\mathbf{v}^n = \frac{3}{2}\mathbf{v}^n - \frac{1}{2}\mathbf{v}^{n-1} \approx \mathbf{v}^{n+\frac{1}{2}}.$$

Multiplying (71) by $2R$ and defining $\tau = 2R/\Delta t$, we see that (71) can be written

$$\begin{aligned} \tilde{a}(\mathbf{v}^{n+1}, \mathbf{z}) &= F^n(\mathbf{z}) \quad \forall \mathbf{z} \in V_h, \\ F^n(\mathbf{z}) &= \tau\,(\mathbf{v}^n, \mathbf{z}) - a(\mathbf{v}^n, \mathbf{z}) - 2R\,\hat{c}(E\mathbf{v}^n, \mathbf{g}, \mathbf{z}) + 2R\,c(E\mathbf{v}^n, E\mathbf{v}^n, \mathbf{z}). \end{aligned} \qquad (72)$$

Then we use the iterated-penalty method (68) as before, with ρ proportional to τ.

This allowed cheaper and more accurate simulations for $R \geq 10^4$. On the other hand, we required $\Delta t \leq 0.001$ in many cases to obtain stable computations. But this allowed computations on finer meshes as were required for larger Re.

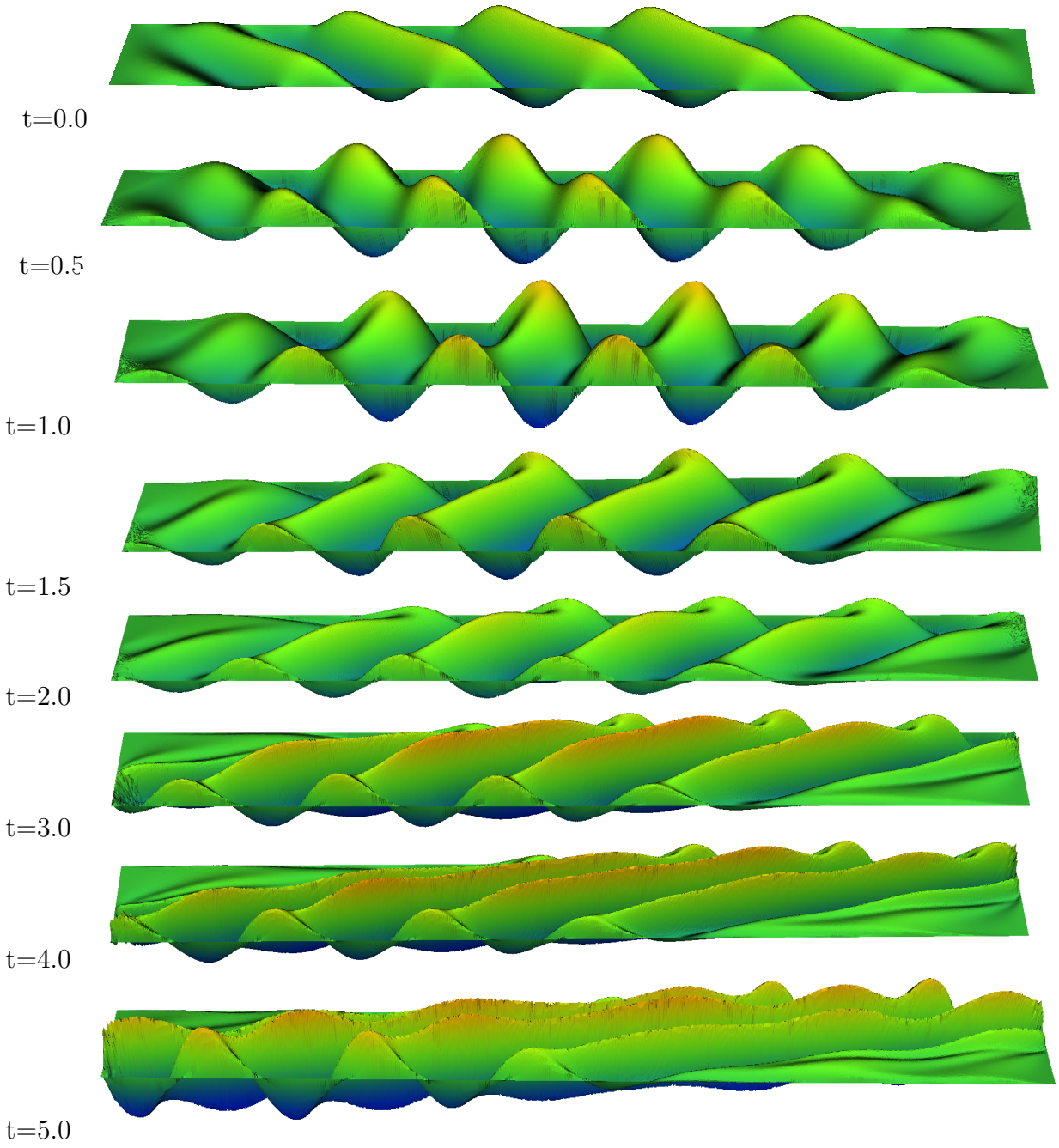

Figure 10: Time series for $R = 1600$. Evolution of perturbation on the domain (2) with $L = 5$ and meshsize parameter $M = 100$, computed using 100 iterations with the initial eigenvector approximation (42) with $\omega = 3.77$. The time-stepping scheme used was the first-order scheme described in section 8.4 with $\Delta t = 0.001$.

R	1600	3000	10000	30000	100000
$T_{\max}$	1.01	1.06	1.13	1.21	1.36
T_P	2.23	2.98	4.21	6.73	9.30
Δt	2.5×10^{-3}	2.5×10^{-3}	1×10^{-3}	1×10^{-3}	5×10^{-4}
M	100	120	150	150	250
U	0.0273	0.0318	0.0420	0.0530	0.0688

Table 5: Time $T_{\max}$ of maximal perturbation as a function of Reynolds number R and the corresponding value of Δt (for the second-order scheme) and meshsize parameter M for the computations as in Figure 11. T_P is the persistence time defined in (65) and $U = \|\nabla \mathbf{u}(t = T_{\max})\|_{L^2(\Omega)}$.

8.7 Interpreting the meshsize parameter M

We utilized the FEniCS Project code `dolfin` for all of the computations, and the meshes were generated with `mshr` [2]. What we refer to as the meshsize parameter M is the input to `mshr`. We can visualize what this means in Figure 13 which depicts the domain (2) with $L = 5$ and $M = 100$. Shown is the horizontal flow component of the approximate eigenvector after five iterations of the power-method. The view is from the underside compared to the standard views which appear in other figures, to emphasize the mesh.

Figure 14 illustrates the impact of meshsize M on a time-dependent computation. Shown is the same computation as done in Figure 11(b), but with 5 different meshsize parameters M. For $M = 50$, we get the tantalizing impression that the instability may be persistent in time, being self-sustaining [44]. But reducing the meshsize unfortunately disabuses us of this fantasy.

The initial doubling of the mesh parameter (from $M = 50$ to $M = 100$) has the biggest impact, with subsequent increases reaching a point of diminishing returns. Note that the finer meshes lead to a sharpening of the peak in the perturbation, making it higher but also making it reach its maximum sooner. In all candor, the curve for $M = 250$ is likely not yet converged. For smaller Reynolds numbers, we confirmed convergence by doing slightly larger computations.

In Figure 15, we compare the horizontal flow patterns for perturbations at $t = 1$ for various Reynolds numbers. We see little difference in form. The amplitude differences given in Table 5 are more significant. The main issue we see with regard to mesh refinement is the sharp boundary layer on the channel walls. We see how this develops in Figure 10 and then persists for $t \geq 1$. Eventually, boundary-layer issues also develop at the ends of the channel. For more detail on the boundary layer, see Figure 16.

Due to the substantial requirements for spatial accuracy, we investigated using specialized meshes. Malkus splits [27] are based on quadrilateral decompositions of a domain. These can be generated in `doflin` for the domain in (2) with the command

```
RectangleMesh(Point(-L, 0.0), Point(L, 1.0), mx, my,'crossed')
```

This will generate a base rectangular decomposition with `mx` rectangles in the x-direction and `mx` rectangles in the y-direction.

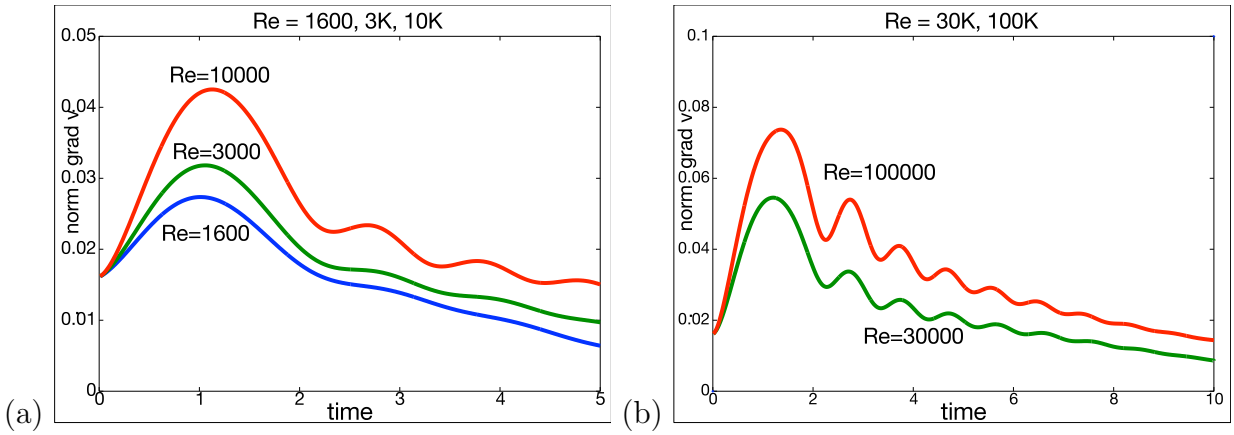

Figure 11: Behavior of the solution $\mathbf{v}$ of the perturbation equations (7) on the domain (2) with $L = 5$. Shown is variation in time of the norm $\|\nabla \mathbf{v}\|_{L^2(\Omega)}$ using an initial perturbation computed using 100 iterations with the initial eigenvector approximation (42) using frequency $\omega = 3.77$. (a) $R = 1600$, $R = 3000$, and $R = 10000$, computed with the scheme (67) together with the iterated-penalty method (68) with meshsize parameter $M = 100$ and Δt as indicated in Table 5. (b) $R = 30000$ and $R = 100000$, computed with the scheme (71) together with the iterated-penalty method (72) with meshsize parameter $M = 50$ and Δt as indicated in Table 5.

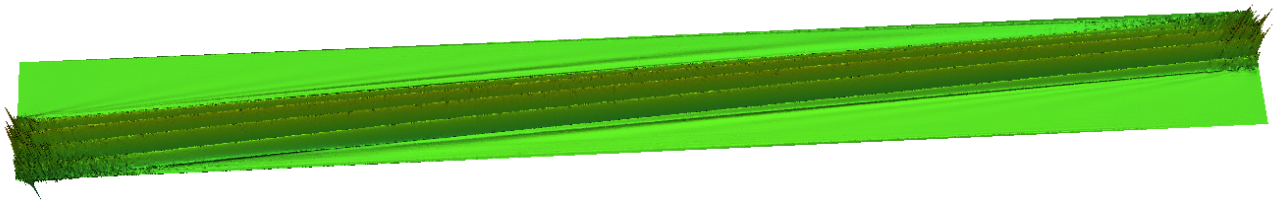

Figure 12: Perturbation at $t = 10$ for $R = 10^5$ computed with the second-order scheme with $\Delta t = 0.0005$ and $M = 250$.

In the general case, each quadrilateral is triangulated by adding the diagonals of the quadrilateral, giving an overall triangulation of the domain. In our case, we used squares. The meshsize parameter m in Table 6 for Malkus splits is the number of squares in the y direction. The number of the squares in the x-direction was thus $2mL$. In Table 6, we report some simulations using Malkus splits. Although the Malkus splits are quite effective for the eigenproblem solution, as indicated in Table 6, their use in time-stepping simulations did not provide a substantial improvement in efficiency.

In Figure 16, we depict the perturbations at $t = 1$ for $R = 1600$ and $R = 10^4$ both computed using Malkus splits with different mesh parameters m. This form of visualization allows the assessment of the width of the boundary layer, because each dot represents a particular unknown in the mesh. The mesh for $R = 10^4$ has twice as many nodal points in each direction, and yet fewer points in the boundary layer. Thus we see how the boundary layer is getting narrower as the Reynolds number R increases. Note that the horizontal row of dots is on the boundary.

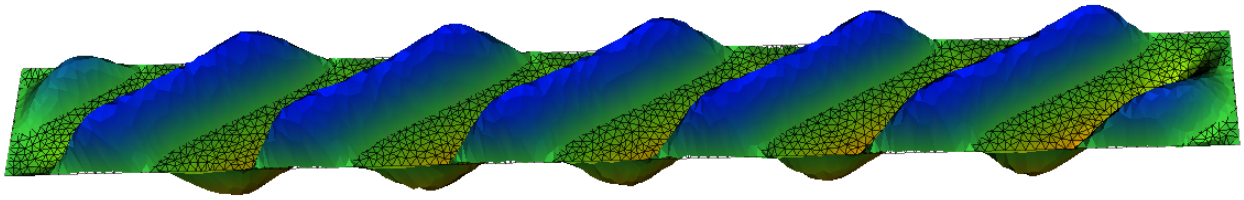

Figure 13: Illustration of meshsize parameter $M = 100$ using `mshr` [2] on the domain (2) with $L = 5$.

L	start vector	λ	iterations	m
5	**v** in (42)	-0.0112168	100	2
5	**v** in (42)	-0.0112206	100	5
5	**v** in (42)	-0.0112206	100	10
5	**v** in (42)	-0.0112206	100	20
5	**v** in (42)	-0.0112216	200	5
5	**v** in (42)	-0.0112216	200	10
10	**v** in (42)	-0.0112684	200	10

Table 6: Using Malkus splits to study dependence on channel length parameter L of stability limits λ; compare Table 1. The "start vector" refers to the initial eigenvector approximation. The iterations column lists the number of iterations used. The meshsize parameter m for Malkus splits is the number of squares in the y direction. The number of the squares in the x-direction was thus $2mL$. For start vectors in (42), the default frequency $\omega = 3.77$ was used. The shift $\mu = 0.01$ in all cases.

8.8 Kinetic versus strain energy

Our theory of instability was based on kinetic energy, but so far we have reported the behavior of strain energy. The time-dependent behavior of kinetic energy is more prosaic, nearly independent of Reynolds number. Figure 17 depicts the latter.

8.9 Numerical instabilities

The time-stepping schemes in sections 8.4 and 8.6 are not inherently stable. Their stability relies on accuracy (staying close to the true solution). As remarked in section 8.4, it is critical to keep essentially exact divergence-zero to avoid instability. But in addition, instability arises if the mesh size and time-step size are not sufficiently small. Figure 18 gives some examples that occur for $R \geq 10^4$.

We see that instabilities can occur at different times, and they can occur for both the first-order scheme in section 8.4 and the second-order scheme in section 8.6. In the former case, stability is recovered by the second-order scheme for a significantly larger time step.

There are some relationships between the time-step size and the meshsize to determine numerical stability. Of course, reducing the time step always improves stability. But reducing

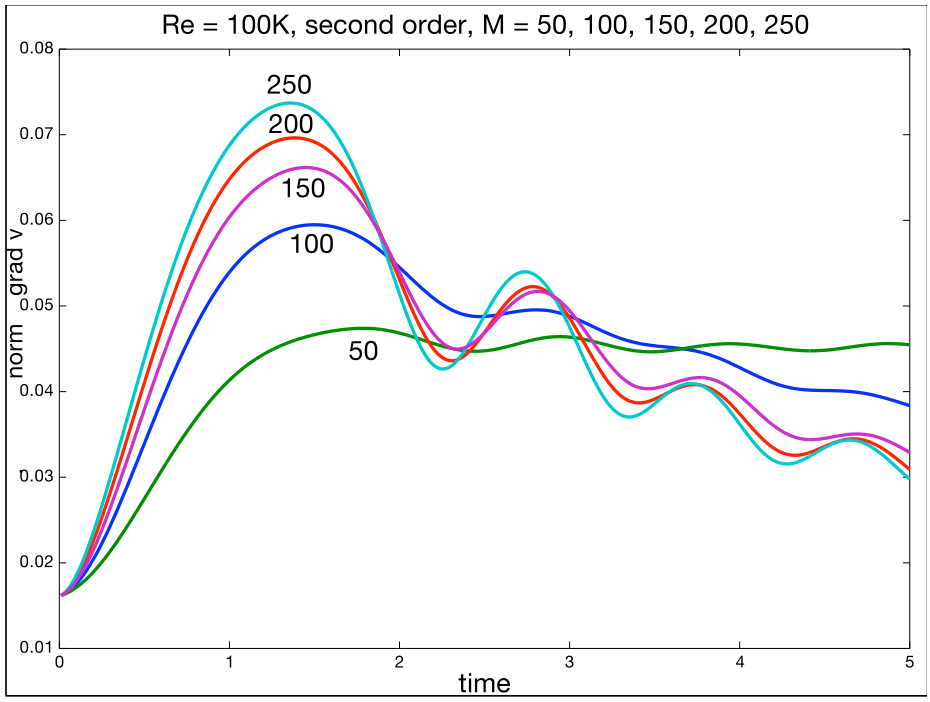

Figure 14: Mesh dependencies for $R = 10^5$. For $M = 50$, computed with the first-order time-stepping scheme in section 8.4 with $\Delta t = 0.0001$. For $M \geq 100$, computed with the second-order time-stepping scheme in section 8.6 with $\Delta t = 0.001$ for $M = 100, 150$ and $\Delta t = 0.0005$ for $M = 200, 250$.

the spatial mesh size may not. For example, for $R = 10^5$, $M = 150$ is stable for $\Delta t = 0.001$ (this is depicted in the middle curve in Figure 14), whereas $M = 200$ is not stable for this time step. Thus the coarser mesh introduces some numerical dissipation that stabilizes the time-stepping scheme.

8.10 Not the worst

The dynamic development of the most unstable mode has been addressed via several simulations in the previous sections. One might hope that some sort of order would appear from this. For example, it might be conjectured that, starting with the most unstable mode would lead to the perturbation that would grow the most and be the most persistent. Unfortunately, this is not the case.

In Figure 19, we depict the evolution for two similar perturbations for $R = 3000$, both seeded with an initial perturbation generated by 100 steps of fixed-point iteration, but each started with a different initial eigenvector approximation of the form (42) but with two different frequencies, $\omega = 3.77$ (see Figure 4) and $\omega = 1$ (see Figure 20).

Comparing Figure 4, we see that the initial perturbation in Figure 20 is not so different. It is the less exact mode in Figure 20 that leads to the the largest growth and persistence time in Figure 19. Thus small variations can have a significant impact on the dynamic evolution of initial perturbations.

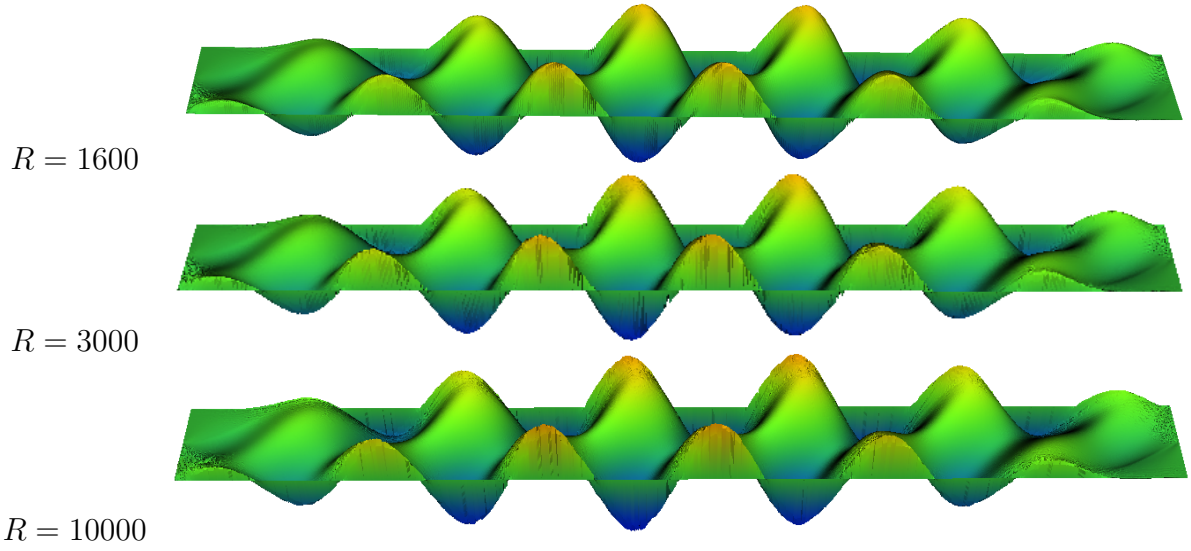

Figure 15: Horizontal flow profile for different Reynolds numbers at time $t = 1$. Evolution of perturbation on the domain (2) with $L = 5$, starting with the eigenvector computed using 100 iterations with the initial eigenvector approximation (42) with $\omega = 3.77$. For $R = 1600$, the time-stepping scheme used was the first-order scheme described in section 8.4 with $\Delta t = 0.001$. For the others, the time-stepping scheme used was the second-order scheme described in section 8.6 with $\Delta t = 0.0025$ for $R = 3000$ and $\Delta t = 0.001$ for $R = 10000$.

9 Energy stability comparisons

There are many definitions of instability [10], and we have not attempted to compare them all. But we can relate some details of the energy stability/instability definition to other concepts. The most important comparison is with the standard definition of instability by a linear analysis.

9.1 Linearization

The standard approach to flow stability [34, 17] has been to consider the linearization of (7). This has been widely used. For example, Chandrasekhar states [6, page 3] "in this book we shall be concerned only with the linear stability theory."

The linear stability analysis is based on an equation obtained from (7) by dropping the nonlinear (quadratic) term in $\mathbf{v}$. We denote by $\tilde{\mathbf{v}}$ the solution of the resulting linear equation:

$$\begin{aligned} R\tilde{\mathbf{v}}_t - \Delta\tilde{\mathbf{v}} + R\big(\mathbf{u}\cdot\nabla\tilde{\mathbf{v}} + \tilde{\mathbf{v}}\cdot\nabla\mathbf{u}\big) + \nabla\tilde{o} = \mathbf{0} \text{ in } \Omega. \\ \nabla\cdot\,\tilde{\mathbf{v}} = 0 \text{ in } \Omega, \quad \tilde{\mathbf{v}} = \mathbf{0} \text{ on } \partial\Omega, \end{aligned} \tag{73}$$

The idea of the linear instability analysis is to look for a solution of (73) of the form

$$\tilde{\mathbf{v}}(t) = e^{\lambda t}\,\tilde{\mathbf{v}}_0.$$

We see that this generates an eigenproblem for $\mathbf{v}_0$ and λ, as follows.

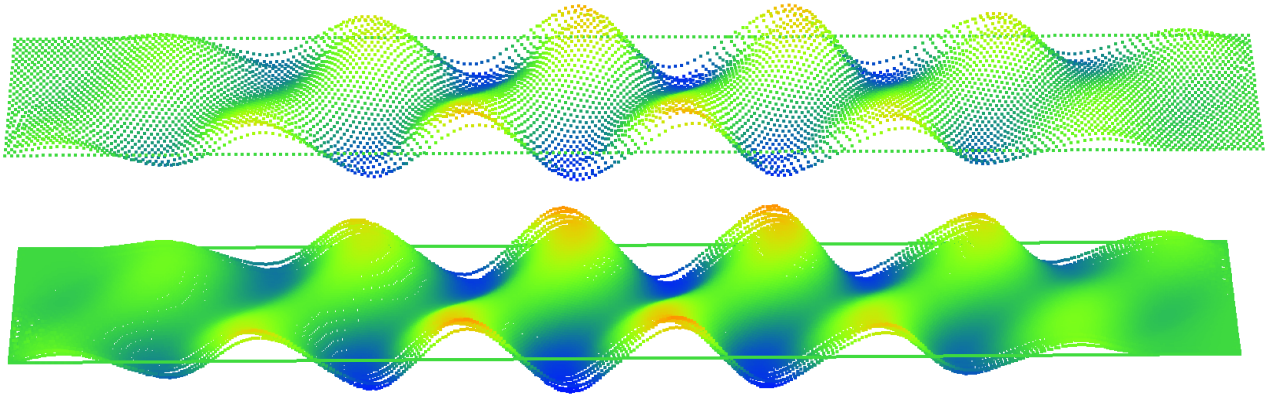

Figure 16: Perturbation at $t = 1$ computed using Malkus splits with the second-order scheme for (top) $R = 1600$ with $m = 5$ and $\Delta t = 0.0025$ and (bottom) $R = 10000$ with $m = 10$ and $\Delta t = 0.001$.

Write the spatial operator in (73) as

$$A_R^{\mathbf{u}}\tilde{\mathbf{v}} = P\big(-\Delta\tilde{\mathbf{v}} + R(\mathbf{u}\cdot\nabla\tilde{\mathbf{v}} + \tilde{\mathbf{v}}\cdot\nabla\mathbf{u})\big), \tag{74}$$

where P is the projection onto the space V, defined in (12), of divergence-free, vector-valued functions that vanish on the boundary and are in the Sobolev space $H^1(\Omega)^d$. Then there is a solution of (73) of the form $\tilde{\mathbf{v}}(t) = e^{\lambda t}\mathbf{v}_0$ if there is an eigensolution of

$$A_R^{\mathbf{u}}\tilde{\mathbf{v}}_0 = \lambda\tilde{\mathbf{v}}_0.$$

Note how this differs from energy instability. In the linear stability analysis, the form of the instability does not change, it just grows. In energy stability analysis, the perturbation is not constrained in this way.

Let $m(R)$ denote the supremum of the real parts of the spectrum of the operator $A_R^{\mathbf{u}}$ defined in (74). It is known [32] that for Couette flow

$$m(R) \le -C/R$$

for a constant $C > 0$. Based on this, it has been concluded that Couette flow is stable for all R. We have seen, by a different approach, that this is not the case. We now explore the differences in approaches in more detail.

9.2 Energy stability versus linear stability analysis

There is not a simple relationship between linear stability analysis, based on the eigenstructure of the operator $A_R^{\mathbf{u}}$ in (74), and energy stability, even though certain ingredients of the analysis are related. Let us write

$$A_R^{\mathbf{u}} = -P(\Delta + R\mathbf{u}\cdot\nabla + RB^{\mathbf{u}}),$$

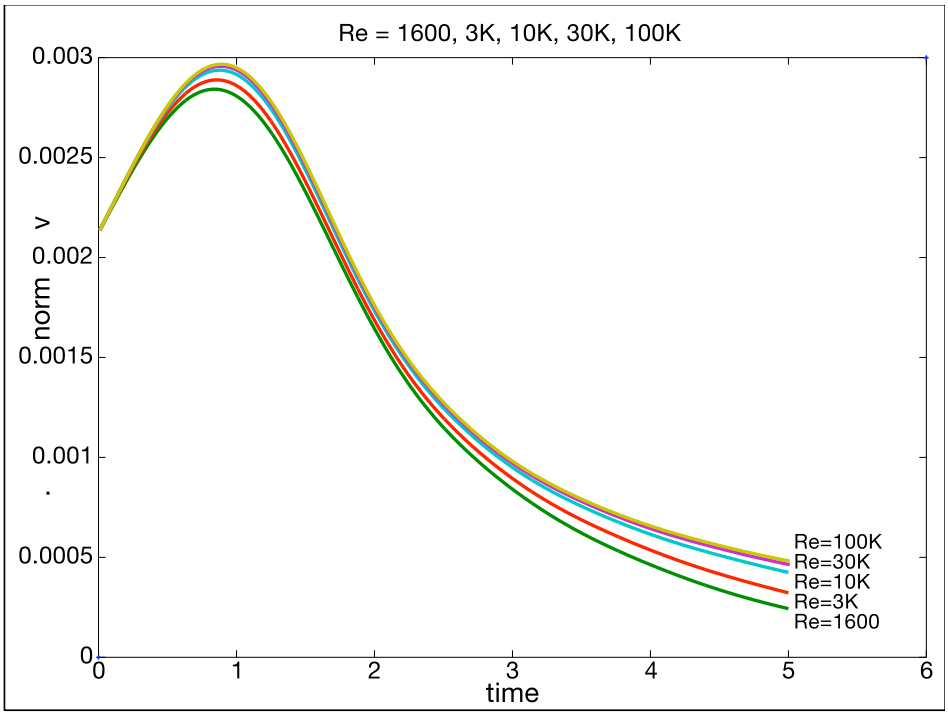

Figure 17: Variation in time of the kinetic energy $\|\mathbf{v}\|_{L^2(\Omega)}$ of the solution $\mathbf{v}$ of the perturbation equations (7) on the domain (2) with $L = 5$ using the schemes indicated in Figure 11.

where $B^{\mathbf{u}}$ is defined by

$$B^{\mathbf{u}}\mathbf{v} = \mathbf{v} \cdot \nabla \mathbf{u}$$

and P is the projection onto V, the space defined in (12). The eigenvalue problem for linear stability analysis is

$$A_R^{\mathbf{u}}\mathbf{v} = \mu \mathbf{v}. \tag{75}$$

By contrast, the eigenvalue problem for energy stability can be written as

$$-\tfrac{1}{2}P(\Delta)^{-1}\big(B^{\mathbf{u}} + (B^{\mathbf{u}})^t\big)\mathbf{v} = \lambda \mathbf{v}.$$

Clearly, $A_R^{\mathbf{u}}$ and $-\tfrac{1}{2}P(\Delta)^{-1}\big(B^{\mathbf{u}} + (B^{\mathbf{u}})^t\big)$ are not related in a simple way. And at the most simplistic level, for energy instability, we are looking for $\lambda < 0$, whereas for eigenvalue instability, we are looking for $\mu > 0$. At the next level, linear stability analysis can lead to eigenproblems for nonnormal operators, whereas nonlinear (energy) stability analysis leads an eigenproblems for a symmetric operator.

Although there is no obvious connection between the two instability criteria, if there is an eigensolution

$$A_R^{\mathbf{u}}\mathbf{v} = -P(\Delta + R\mathbf{u} \cdot \nabla + RB^{\mathbf{u}})\mathbf{v} = \mu \mathbf{v}, \tag{76}$$

arising from linear (eigenvalue) instability analysis, then we can take the L^2 inner-product with $\mathbf{v}$ to get

$$-\int_\Omega |\nabla \mathbf{v}|^2 \, d\mathbf{x} - \frac{R}{2}\int_\Omega \mathbf{v}^t\big(\nabla \mathbf{u} + \nabla \mathbf{u}^t\big)\mathbf{v} \, d\mathbf{x} = \mu \int_\Omega |\mathbf{v}|^2 \, d\mathbf{x},$$

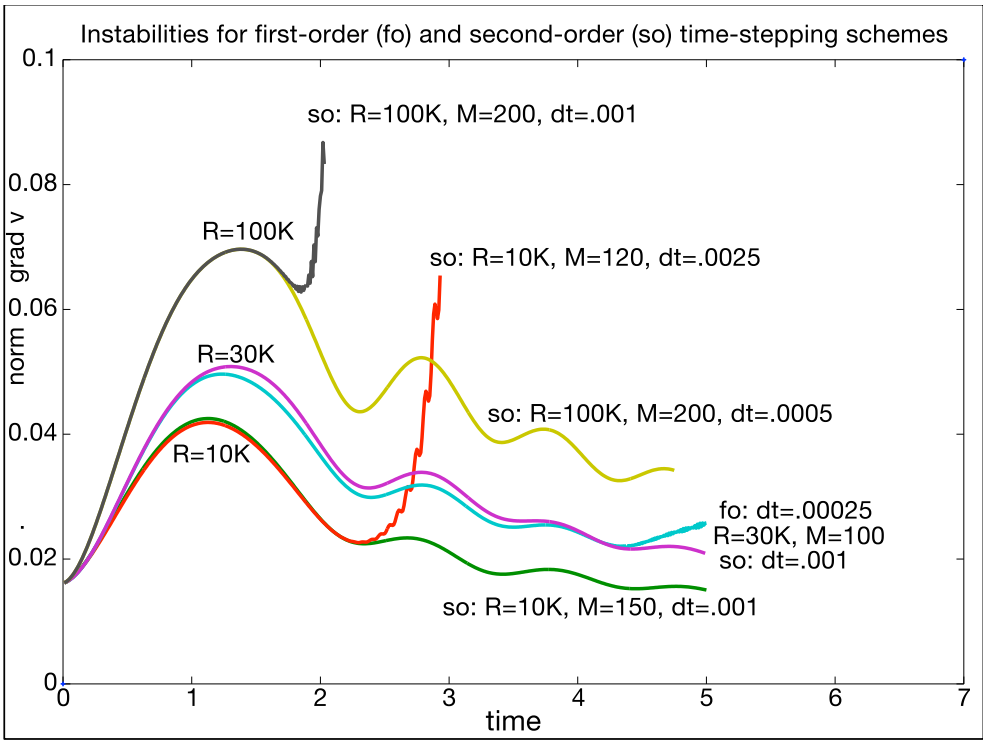

Figure 18: Instabilities for $R = 10^4$, 3×10^4, 10^5 for the time-stepping schemes in sections 8.4 and 8.6. Shown is variation in time of the norm $\|\nabla \mathbf{v}\|_{L^2(\Omega)}$ of the solution $\mathbf{v}$ of the perturbation equations (7) on the domain (2) with $L = 5$ using the schemes indicated started with an initial perturbation computed using 100 iterations with the initial eigenvector approximation (42) using frequency $\omega = 3.77$.

after simplifications as done in the derivation of (10).

Thus an eigenvector $\mathbf{v}$ for (76), characterizing linear (eigenvalue) instability, implies energy instability if $\mu > 0$, but $\mathbf{v}$ is not necessarily the most unstable mode given by the eigenproblem (20). Nor is it even necessarily any eigenvector of the eigenproblem (20). Therefore eigenvalue (linear) instability implies energy instability, but not conversely. Moreover, eigenvalue (linear) stability analysis suggests an instability at a particular Reynolds number, somewhat like bifurcation analysis [1, 8]. By contrast, energy instability implies instability for all Reynolds numbers above a certain threshold, at least in the case that the base flow $\mathbf{u}$ does not depend on R.

The nonlinear (energy) analysis is (1) exact and (2) more general. It captures all of the unstable modes, not just special ones. There are no approximations.

If you have some perturbation $e^{ct}\mathbf{v}$ coming from (75), is not so easy to prove that adding such a perturbation gives a (nearby) solution of Navier-Stokes. To do so would require some sort of stability of the base flow. But if the base flow is unstable, then the reasoning is contradictory. The basic argument of linear stability analysis can be written as

$$\text{eigensolution (75)} + \text{stability} \implies \text{instability}.$$

So it is fundamentally flawed. It is understandable how such finer points of logic might have

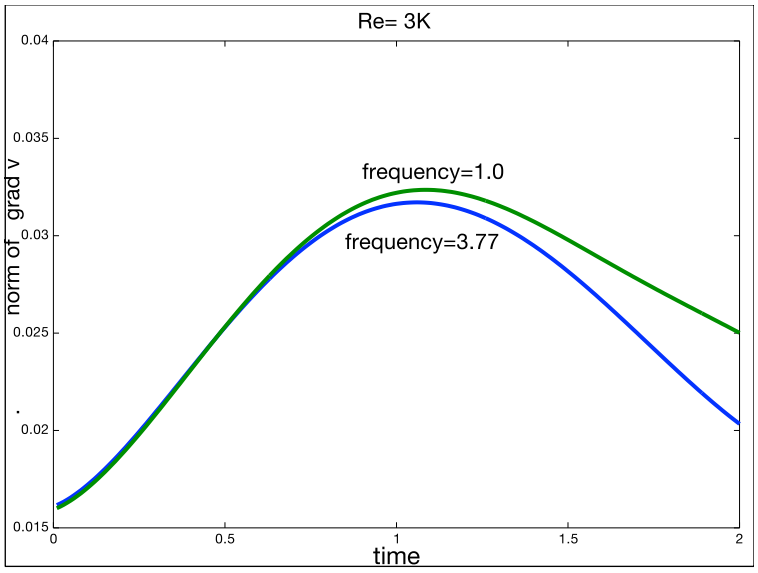

Figure 19: Behavior of the solution $\mathbf{v}$ of the perturbation equations (7) on the domain (2) with $L = 5$ and meshsize parameter $M = 100$, using the scheme (67), together with the iterated-penalty method (68). Shown is variation in time of the norm $\|\nabla \mathbf{v}\|_{L^2(\Omega)}$ using an initial perturbation computed using 100 iterations with the initial eigenvector approximation (42) using two different frequencies, $\omega = 1$ and $\omega = 3.77$, for $R = 3000$ and $\Delta t = 2.5 \times 10^{-4}$.

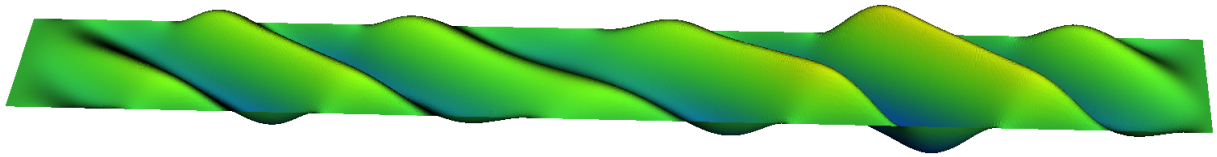

Figure 20: The initial perturbation on the domain (2) with $L = 5$ and meshsize parameter $M = 100$, computed using 100 iterations with the initial eigenvector approximation (42) with $\omega = 1$.

been spurned as mathematical rigor mortis [33], but in this case it clearly gave the wrong result.

9.3 Energy stability versus Newton's method

Newton's method for solving the stationary Navier-Stokes equations [36, section 20.3] involves inversion of the system associated with the variational form

$$a(\mathbf{v}, \mathbf{w}) + R\,\hat{c}(\mathbf{u}, \mathbf{v}, \mathbf{w}), \tag{77}$$

where

$$\hat{c}(\mathbf{u}, \mathbf{w}, \mathbf{v}) = c(\mathbf{u}, \mathbf{w}, \mathbf{v}) + c(\mathbf{w}, \mathbf{u}, \mathbf{v}),$$

and $c(\mathbf{u}, \mathbf{w}, \mathbf{v})$ is defined in (8). Moreover [36, (20.35)]

$$\hat{c}(\mathbf{u}, \mathbf{v}, \mathbf{v}) = \mathcal{B}_{\mathbf{u}}(\mathbf{v}, \mathbf{v}) \quad \forall \mathbf{v} \in V. \tag{78}$$

where the bilinear form $\mathcal{B}_{\mathbf{u}}(\mathbf{v},\mathbf{v})$ was defined in (14). If the Newton system (77) is singular, then there is a $\mathbf{v} \in V$ such that

$$a(\mathbf{v},\mathbf{w}) + R\,\hat{c}(\mathbf{u},\mathbf{v},\mathbf{w}) = 0 \quad \forall \mathbf{w} \in V. \tag{79}$$

Choosing $\mathbf{w} = \mathbf{v}$ and combining (78) and (79), we find that

$$a(\mathbf{v},\mathbf{v}) + R\,\mathcal{B}_{\mathbf{u}}(\mathbf{v},\mathbf{v}) = 0.$$

Thus singularity of the system (77) corresponds to an eigenvalue of (20) equal to

$$\lambda = -2/R.$$

Singularity of the Newton system often corresponds to a bifurcation [1, 8].

10 Function space view

What we have done is to construct a function F given by

$$F(\mathbf{u}) = (\mathbf{v}_{\mathbf{u}}, \lambda_{\mathbf{u}})$$

for all $\mathbf{u} \in V + \mathbf{g}$, where $(\mathbf{v}_{\mathbf{u}}, \lambda_{\mathbf{u}})$ solves the eigenproblem (20). We can define the unstable set $V_{\mathbf{g}}^U$ by

$$V_{\mathbf{g}}^U = \{\mathbf{u} \in V + \mathbf{g} \ : \ \lambda_{\mathbf{u}} < 0\}.$$

Then we have divided $V + \mathbf{g}$ into two sets, $V_{\mathbf{g}}^U$ and its complement, the latter being the stable set. In the time-dependent calculations for Couette flow, we initially get a solution near $\mathbf{u}+\epsilon\mathbf{v}_{\mathbf{u}}$. It is thus natural to ask about $F(\mathbf{u}+\epsilon\mathbf{v}_{\mathbf{u}})$ to see if it indicates greater instability or less instability. In the time-dependent calculations for Couette flow, it appears to be more unstable initially. If F is sufficiently smooth, we can write

$$F(\mathbf{u} + \epsilon\mathbf{v}_{\mathbf{u}}) = (\mathbf{v}_{\mathbf{u}} + \epsilon\mathbf{v}', \lambda_{\mathbf{u}} + \epsilon\lambda') + \mathcal{O}\left(\epsilon^2\right).$$

If $\lambda' < 0$, then the instability is increasing. The easiest way to compute λ' may be to just solve the time-dependent Navier-Stokes equations. But this is a standard eigenvalue perturbation problem, so it is possible to determine equations for $\mathbf{v}'$ and λ', as follows.

Suppose that

$$A^{-1}B_{\mathbf{u}}\mathbf{v} = \lambda\mathbf{v}$$

and

$$A^{-1}B_{\mathbf{u}+\epsilon\mathbf{v}}(\mathbf{v} + \epsilon\mathbf{v}') = (\lambda + \epsilon\lambda')(\mathbf{v} + \epsilon\mathbf{v}') + \mathcal{O}\left(\epsilon^2\right).$$

Note that

$$B_{\mathbf{u}+\epsilon\mathbf{v}} = B_{\mathbf{u}} + B_{\epsilon\mathbf{v}} = B_{\mathbf{u}} + \epsilon B_{\mathbf{v}}.$$

Therefore

$$\begin{aligned} A^{-1}B_{\mathbf{u}+\epsilon\mathbf{v}}(\mathbf{v} + \epsilon\mathbf{v}') &= A^{-1}B_{\mathbf{u}}\mathbf{v} + \epsilon\big(A^{-1}B_{\mathbf{v}}\mathbf{v} + A^{-1}B_{\mathbf{u}}\mathbf{v}'\big) + \epsilon^2 A^{-1}B_{\mathbf{v}}\mathbf{v}' \\ &= \lambda\mathbf{v} + \epsilon\big(A^{-1}B_{\mathbf{v}}\mathbf{v} + A^{-1}B_{\mathbf{u}}\mathbf{v}'\big) + \epsilon^2 A^{-1}B_{\mathbf{v}}\mathbf{v}'. \end{aligned} \tag{80}$$

Similarly

$$(\lambda + \epsilon\lambda')(\mathbf{v} + \epsilon\mathbf{v}') = \lambda\mathbf{v} + \epsilon\big(\lambda'\mathbf{v} + \lambda\mathbf{v}'\big) + \epsilon^2\lambda'\mathbf{v}'. \tag{81}$$

Equating terms of order ϵ, we find

$$A^{-1}B_{\mathbf{v}}\mathbf{v} + A^{-1}B_{\mathbf{u}}\mathbf{v}' = \lambda'\mathbf{v} + \lambda\mathbf{v}'$$

which we can re-write as

$$A^{-1}B_{\mathbf{u}}\mathbf{v}' - \lambda\mathbf{v}' = \lambda'\mathbf{v} - A^{-1}B_{\mathbf{v}}\mathbf{v}. \tag{82}$$

Equation (82) is uniquely solvable in the set

$$V_{\mathbf{v}} = \{\mathbf{w} \in V \ : \ (\mathbf{v}, \mathbf{w}) = 0\},$$

provided that λ is a simple eigenvalue of $A^{-1}B_{\mathbf{u}}$ and

$$(\lambda'\mathbf{v} - A^{-1}B_{\mathbf{v}}\mathbf{v}, \mathbf{v}) = 0.$$

Thus

$$\lambda' = \frac{(A^{-1}B_{\mathbf{v}}\mathbf{v}, \mathbf{v})}{(\mathbf{v}, \mathbf{v})}.$$

This can be computed by solving $A\mathbf{w} = B_{\mathbf{v}}\mathbf{v}$ and setting

$$\lambda' = \frac{(\mathbf{w}, \mathbf{v})}{(\mathbf{v}, \mathbf{v})}.$$

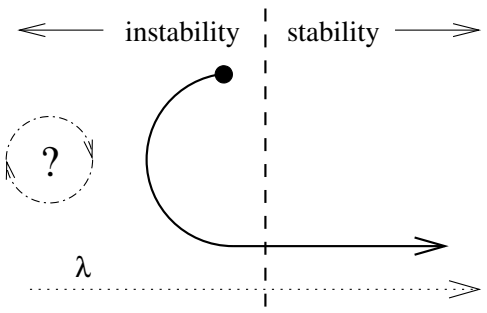

Figure 21: Cartoon of the time-dependent behavior of the instability for Couette flow. The dashed line indicates the boundary between the stable ($\lambda > 0$) and unstable ($\lambda < 0$) regions.

In Figure 21, we depict what happens with the instability for Couette flow. Initially, the perturbation grows, indicating that $\lambda' < 0$. But then the perturbation saturates, and it eventually dissipates to zero. In the figure, the large black dot indicates the initial perturbation, and the curve attached to it indicates the time evolution of the perturbation. Initially, it moves to the left, where solutions are more unstable. But then it turns around and moves toward the stable region. At some point it passes the dashed line indicating the boundary between the stable and unstable regions.

With this function-space view of the evolution of instabilities, an intriguing possibility would be a cycle in the unstable region, indicated by the dot-dashed curve surrounding the question mark in Figure 21. This would indicate an instability that, once initiated, would continue to cycle forever, that is, one that is self-sustaining [44].

Another space of functions potentially of interest are the steady solutions of Navier-Stokes:

$$V_{\mathbf{g},R} = \left\{ \mathbf{u} \in V + \mathbf{g} \ : \ -\Delta \mathbf{u} + R\mathbf{u} \cdot \nabla \mathbf{u} \in \nabla L^2(\Omega) \right\}.$$

Then the unstable steady solutions are

$$V^U_{\mathbf{g},R} = \left\{ \mathbf{u} \in V_{\mathbf{g},R} \ : \ \lambda_{\mathbf{u}} < -2/R \right\}.$$

For a given $\mathbf{g}$, a set of solutions $\mathbf{u}_R$ could go in and out of the unstable set as R varies. This is because the set $V^U_{\mathbf{g},R}$ is changing as R varies.

11 Three-dimensional perturbations

Couette flow and plane Poiseuille flow are exact models of three-dimensional flows that are independent of the third coordinate. Other important flow problems are also of this form. The unstable modes found via a two-dimensional analysis thus also represent flows that are constant in the third coordinate. But what if we pose them as three-dimensional flow problems, relaxing the requirement that the instabilities be independent of the third coordinate? What sort of instabilities arise in this case? Do they occur for lower Reynolds numbers? Such questions are addressed here.

Couette flow and plane Poiseuille flow represent flow domains that are infinite in the third coordinate. For computational purposes, the third coordinate z must be truncated artificially via $|z| \leq L$. Thus it is of interest to know how such three-dimensional perturbations depend on L. In comparing with experimental results, L would be defined in the experiment. Another approach would be to look for modes that are periodic in the third dimension, with period L. We can then ask:

- how does the smallest eigenvalue depend on L?
- for what L is the smallest eigenvalue minimized?
- or does it occur that the most unstable mode in three dimensions is actually independent of the third coordinate?

We will show that in some cases the most unstable mode in three dimensions is actually two-dimensional. In particular, we will show that this is true for Couette flow, so we have found the most unstable, three-dimensional perturbation already.

Given the general importance of these questions, we will generalize beyond Couette flow. We will still restrict to base flows $\mathbf{u}$ that are two-dimensional. Thus the general form of such flows has strain rate given by

$$\nabla \mathbf{u} + \nabla \mathbf{u}^t = \begin{pmatrix} a(x,y) & b(x,y) & 0 \\ b(x,y) & -a(x,y) & 0 \\ 0 & 0 & 0 \end{pmatrix} \tag{83}$$

if $\nabla\cdot\,\mathbf{u}=0$. Here we focus on the case $a\equiv 0$, with

$$\mathcal{B}(\mathbf{v},\mathbf{w})=\int_\Omega (v_x w_y+v_y w_x)b(x,y)\,d\mathbf{x}. \tag{84}$$

Generalizing (15), we consider the eigenvalue problem

$$\lambda=\inf_{\mathbf{0}\neq\mathbf{v}\in V}\frac{\int_\Omega (v_x w_y+v_y w_x)b(x,y)\,d\mathbf{x}}{a(\mathbf{v},\mathbf{v})}, \tag{85}$$

We will be more precise about the domain of integration, and the number of variables, in the subsequent discussion.

11.1 Eigenproblem structure

Having the third component v_z nonzero contributes nothing to the numerator in (15), or more generally in (85), so the most unstable modes would be expected to be of the form $\mathbf{v}=(v_x,v_y,0)$. The formal proof of this can be done by introducing an appropriate subspace of the space V^3 defined in (12):

$$V_2=V_2^3=\left\{\mathbf{v}\in V^3\ :\ v_z\equiv 0\right\}. \tag{86}$$

Let $P:V\to V_2$ be the projection defined by

$$P(v_x,v_y,v_z)=(v_x,v_y,0).$$

These definitions make sense for dimension $d=2$ and $d=3$, but the main significance is the case $d=3$. Note that

$$\begin{aligned}\int_\Omega |\nabla(P\mathbf{v})|^2\,d\mathbf{x}&=\int_\Omega |\nabla v_x|^2+|\nabla v_y|^2\,d\mathbf{x}\\ &\le\int_\Omega |\nabla v_x|^2+|\nabla v_y|^2+|\nabla v_z|^2\,d\mathbf{x}=\int_\Omega |\nabla\mathbf{v}|^2\,d\mathbf{x},\end{aligned} \tag{87}$$

where now Ω is assumed to be a three-dimensional domain. When $\lambda<0$

$$\begin{aligned}\lambda&=\inf_{\mathbf{0}\neq\mathbf{v}\in V}\frac{\int_\Omega \mathbf{v}^t(\nabla\mathbf{u}_0+\nabla\mathbf{u}_0^t)\mathbf{v}\,d\mathbf{x}}{\int_\Omega|\nabla\mathbf{v}|^2\,d\mathbf{x}}=\inf_{\mathbf{0}\neq\mathbf{v}\in V}\frac{\int_\Omega (P\mathbf{v})^t(\nabla\mathbf{u}_0+\nabla\mathbf{u}_0^t)(P\mathbf{v})\,d\mathbf{x}}{\int_\Omega|\nabla\mathbf{v}|^2\,d\mathbf{x}}\\ &\ge\inf_{\mathbf{0}\neq\mathbf{v}\in V}\frac{\int_\Omega (P\mathbf{v})^t(\nabla\mathbf{u}_0+\nabla\mathbf{u}_0^t)(P\mathbf{v})\,d\mathbf{x}}{\int_\Omega|\nabla(P\mathbf{v})|^2\,d\mathbf{x}}=\inf_{\mathbf{0}\neq\mathbf{v}\in V_2}\frac{\int_\Omega \mathbf{v}^t(\nabla\mathbf{u}_0+\nabla\mathbf{u}_0^t)\mathbf{v}\,d\mathbf{x}}{\int_\Omega|\nabla\mathbf{v}|^2\,d\mathbf{x}}.\end{aligned} \tag{88}$$

But since $V_2\subset V$, (83) implies

$$\begin{aligned}\inf_{\mathbf{0}\neq\mathbf{v}\in V_2}\frac{\int_\Omega \mathbf{v}^t(\nabla\mathbf{u}_0+\nabla\mathbf{u}_0^t)\mathbf{v}\,d\mathbf{x}}{\int_\Omega|\nabla\mathbf{v}|^2\,d\mathbf{x}}&\le\inf_{\mathbf{0}\neq\mathbf{v}\in V}\frac{\int_\Omega \mathbf{v}^t(\nabla\mathbf{u}_0+\nabla\mathbf{u}_0^t)\mathbf{v}\,d\mathbf{x}}{\int_\Omega|\nabla\mathbf{v}|^2\,d\mathbf{x}}\\ &\le\inf_{\mathbf{0}\neq\mathbf{v}\in V_2}\frac{\int_\Omega \mathbf{v}^t(\nabla\mathbf{u}_0+\nabla\mathbf{u}_0^t)\mathbf{v}\,d\mathbf{x}}{\int_\Omega|\nabla\mathbf{v}|^2\,d\mathbf{x}}.\end{aligned} \tag{89}$$

Therefore

$$\inf_{\mathbf{0}\neq\mathbf{v}\in V_2} \frac{\int_\Omega \mathbf{v}^t(\nabla\mathbf{u}_0+\nabla\mathbf{u}_0^t)\mathbf{v}\,d\mathbf{x}}{\int_\Omega |\nabla\mathbf{v}|^2\,d\mathbf{x}} = \inf_{\mathbf{0}\neq\mathbf{v}\in V} \frac{\int_\Omega \mathbf{v}^t(\nabla\mathbf{u}_0+\nabla\mathbf{u}_0^t)\mathbf{v}\,d\mathbf{x}}{\int_\Omega |\nabla\mathbf{v}|^2\,d\mathbf{x}}.$$

Thus we have proved the following result.

Lemma 11.1 *For two-dimensional base flows, the most unstable mode in the restricted space V_2 results in the same eigenvalue as the general case* (85).

Note that the lemma does *not* say that the most unstable perturbation is independent of z. It just says that it does not point in the z-direction. However, we will now show that perturbations periodic in the z-direction yield the same most-negative eigenvalue when (84) holds.

11.2 Periodic modes

It is natural to look for three-dimensional modes that are periodic in z, with some period, say $2\pi/L$. Thus we can seek

$$\lambda_L^3 = \inf_{\mathbf{0}\neq\mathbf{v}\in V_2^{3,L}} \frac{\int_{\Omega_L} 2v_xv_yb(x,y)\,dx\,dy\,dz}{\int_{\Omega_L}|\nabla\mathbf{v}|^2\,dx\,dy\,dz}, \tag{90}$$

where

$$V_2^{3,L} = \left\{\mathbf{v}\in V_2^3 \;:\; \mathbf{v} \text{ has period } 2\pi/L \text{ in } z\right\}, \quad \Omega_L = \left\{(x,y,z) \;:\; (x,y)\in\Omega,\ |z|\le 2\pi/L\right\}.$$

We contrast (90) with the two-dimensional approximation

$$\lambda^2 = \inf_{\mathbf{0}\neq\mathbf{v}\in V_2^2} \frac{\int_\Omega 2v_xv_yb(x,y)\,dx\,dy}{\int_\Omega|\nabla\mathbf{v}|^2\,dx\,dy}, \tag{91}$$

where V_2^2 is the original space (12) defined on the two-dimensional domain Ω. Note that there is a natural inclusion $V_2^2\subset V_2^{3,L}$ where we view $\mathbf{v}\in V_2^2$ as constant in z. Correspondingly, let us define

$$\begin{aligned}
a^2(\mathbf{v},\mathbf{w}) &= \int_\Omega \nabla\mathbf{v}:\nabla\mathbf{w}\,dx\,dy \quad \forall\mathbf{v},\mathbf{w}\in V^2,\\
a_L(\mathbf{v},\mathbf{w}) &= \frac{L}{2\pi}\int_{\Omega_L}\nabla\mathbf{v}:\nabla\mathbf{w}\,dx\,dy\,dz \quad \forall\mathbf{v},\mathbf{w}\in V_2^{3,L},\\
\mathcal{B}_L(\mathbf{v},\mathbf{w}) &= \frac{L}{2\pi}\int_{\Omega_L}\big(v_xw_y+v_yw_x\big)b(x,y)\,dx\,dy\,dz \quad \forall\mathbf{v},\mathbf{w}\in V_2^{3,L}.
\end{aligned} \tag{92}$$

Note that

$$a_L(\mathbf{v},\mathbf{w}) = a^2(\mathbf{v},\mathbf{w}) \quad \forall\,\mathbf{v},\mathbf{w}\in V_2^2. \tag{93}$$

Since the most unstable mode that is constant in z is in $V_2^{3,L}$,

$$\lambda_L^3\le\lambda^2. \tag{94}$$

For any $\mathbf{v} \in V_2^{3,L}$, we can do a Fourier series expansion

$$\mathbf{v} = \sqrt{\frac{L}{2\pi}}\,\mathbf{v}^0 + \sqrt{\frac{L}{\pi}}\Big(\sum_{k=1}^{\infty} \mathbf{v}^k \cos(kLz) + \mathbf{w}^k \sin(kLz)\Big), \tag{95}$$

where $\mathbf{v}^k, \mathbf{w}^k \in V_2^2$, and $\mathbf{v}^0 = \mathbf{w}^0$. More precisely, we define $\mathbf{v}^k, \mathbf{w}^k \in V_2^2$ by

$$\begin{aligned} \mathbf{v}^k(x,y) &= \sqrt{\frac{L}{\pi}} \int_{-\pi/L}^{\pi/L} \mathbf{v}(x,y,z)\cos(kLz)\,dz, \\ \mathbf{w}^k(x,y) &= \sqrt{\frac{L}{\pi}} \int_{-\pi/L}^{\pi/L} \mathbf{v}(x,y,z)\sin(kLz)\,dz, \end{aligned} \tag{96}$$

for $k > 0$, and

$$\mathbf{v}^0(x,y) = \sqrt{\frac{L}{2\pi}} \int_{-\pi/L}^{\pi/L} \mathbf{v}(x,y,z)\,dz. \tag{97}$$

A key observation is that, for $\mathbf{v} \in V_2^{3,L}$, $\nabla\cdot\mathbf{v} = v_{x,x} + v_{y,y}$ since $v_z \equiv 0$, so each $\mathbf{v}^k$ is divergence free, and so $\mathbf{v}^k \in V_2^2$. Note that for $k > 0$

$$\int_{-\pi/L}^{\pi/L} \frac{L}{\pi}\cos^2(kLz)\,dz = \int_{-\pi/L}^{\pi/L} \frac{L}{\pi}\sin^2(kLz)\,dz = 1.$$

Thus $\mathbf{v}$ has been expanded in an orthonormal basis. If $\lambda^2 \le 0$, then (91) and (93) imply

$$\begin{aligned} -\mathcal{B}_L(\mathbf{v},\mathbf{v}) &= -2\int_\Omega v_x^0\, v_y^0\, b(x,y)\,dx\,dy - 2\sum_{k>0}\int_\Omega \big(v_x^k\, v_y^k + w_x^k\, w_y^k\big)\, b(x,y)\,dx\,dy \\ &\le (-\lambda^2)\Big(a^2(\mathbf{v}^0,\mathbf{v}^0) + \sum_{k>0}\big(a^2(\mathbf{v}^k,\mathbf{v}^k) + a^2(\mathbf{w}^k,\mathbf{w}^k)\big)\Big) \\ &= (-\lambda^2)\Big(a_L(\mathbf{v}^0,\mathbf{v}^0) + \sum_{k>0} a_L(\mathbf{v}^k,\mathbf{v}^k) + \sum_{k>0} a_L(\mathbf{w}^k,\mathbf{w}^k)\Big) \\ &= (-\lambda^2)a_L(\mathbf{v},\mathbf{v}) \end{aligned} \tag{98}$$

Thus we conclude that

$$-\lambda_L^3 \le -\lambda^2. \tag{99}$$

Combining (99) and (94), we have proved the following result.

Theorem 11.1 *Suppose that $\mathcal{B}(\cdot,\cdot)$ is of the form* (84)*. Let λ^2 be the most negative eigenvalue for the two-dimensional eigenvalue problem* (91)*, and let λ_L^3 be the most negative eigenvalue for the three-dimensional eigenvalue problem* (90)*. If $\lambda^2 \le 0$, then*

$$\lambda_L^3 = \lambda^2$$

for any $L > 0$.

11.3 Decaying modes

We can apply the techniques of section 11.2 to perturbations that are not periodic in z. For example, let us consider ones that decay sufficiently fast to be in a Sobolev space. This corresponds in a sense to the limit $L \to 0$ in the periodic problem. Thus we define

$$\lambda_0^3 = \inf_{\mathbf{0}\neq\mathbf{v}\in V_2^3} \frac{\int_{\Omega_0} 2v_x v_y b(x,y)\,dx\,dy\,dz}{\int_{\Omega_0} |\nabla \mathbf{v}|^2\,dx\,dy\,dz}, \tag{100}$$

where

$$\Omega_0 = \{(x,y,z) \ : \ (x,y)\in\Omega,\ z\in\mathbb{R}\}\,. \tag{101}$$

We again contrast (100) with the two-dimensional approximation (91). Note that there is not a natural inclusion $V_2^2 \subset V_2^3$, so we need to replace this concept which was used to prove (94).

Let us begin by abstracting the argument in the periodic case. We choose a complete, orthonormal basis $\{\phi_i \ : \ i = 0, 1, \ldots\}$ in one-dimension and expand $\mathbf{v} \in V_2^3$ via

$$\mathbf{v} = \sum_{k=0}^{\infty} \mathbf{v}^k \phi_k, \tag{102}$$

where $\mathbf{v}^k \in V_2^2$ is defined by

$$\mathbf{v}^k(x,y) = \int_{-\infty}^{\infty} \mathbf{v}(x,y,z)\phi_k(z)\,dz,$$

for $k \geq 0$. For example, we can take the basis functions to be Hermite functions (polynomials multiplied by e^{-z^2}) [14]. Again, for $\mathbf{v} \in V_2^3$, $\nabla\cdot\,\mathbf{v} = v_{x,x} + v_{y,y}$ since $v_z \equiv 0$, so each $\mathbf{v}^k$ is divergence free.

For clarity, let us define, for all $\mathbf{v}, \mathbf{w} \in V_2^3$,

$$\begin{aligned} a_0(\mathbf{v},\mathbf{w}) &= \int_{\Omega_0} \nabla\mathbf{v} : \nabla\mathbf{w}\,dx\,dy\,dz, \\ \mathcal{B}_0(\mathbf{v},\mathbf{w}) &= \int_{\Omega_0} \big(v_x w_y + v_y w_x\big) b(x,y)\,dx\,dy\,dz. \end{aligned} \tag{103}$$

Note that

$$a_0(\mathbf{v},\mathbf{v}) = \sum_{k=0}^{\infty} \int_{\Omega} |v^k_{x,x}|^2 + |v^k_{x,y}|^2 + |v^k_{y,x}|^2 + |v^k_{y,y}|^2\,dx\,dy = \sum_{k=0}^{\infty} a^2(\mathbf{v}^k,\mathbf{v}^k)\,. \tag{104}$$

If $\lambda^2 \leq 0$, then (91) and (104) imply

$$\begin{aligned} -\mathcal{B}_0(\mathbf{v},\mathbf{v}) &= -2\sum_{k\geq 0} \int_{\Omega} v_x^k\, v_y^k\, b(x,y)\,dxdy \leq (-\lambda^2)\sum_{k\geq 0} a^2(\mathbf{v}^k,\mathbf{v}^k) \\ &= (-\lambda^2)\sum_{k\geq 0} a_0(\mathbf{v}^k,\mathbf{v}^k) = (-\lambda^2) a_0(\mathbf{v},\mathbf{v}). \end{aligned} \tag{105}$$

Thus we conclude that $-\lambda_0^3 \le -\lambda^2$, and thus

$$\lambda^2 \le \lambda_0^3. \tag{106}$$

Now we derive a replacement for (94). Define a function χ_ϵ by

$$\chi_\epsilon(z) = \begin{cases} \frac{1}{2}\epsilon & \epsilon|z| \le 1 \\ \frac{1}{2}(1+\epsilon-\epsilon|z|) & 1 \le \epsilon|z| \le 1+\epsilon \\ 0 & \epsilon|z| \ge 1+\epsilon\,, \end{cases} \tag{107}$$

for all $\epsilon > 0$. Note that $|\chi_\epsilon'(z)| \le \frac{1}{2}\epsilon$ for all z. Let $\mathbf{v} \in V_2^2$ be arbitrary (nonzero). Define $\mathbf{v}^\epsilon = \chi_\epsilon \mathbf{v} \in V_2^3$. Then

$$|\nabla \mathbf{v}^\epsilon(x,y,z)|^2 = \begin{cases} \frac{1}{2}\epsilon|\nabla \mathbf{v}(x,y)|^2 & \epsilon|z| \le 1 \\ \frac{1}{2}(1+\epsilon-\epsilon|z|)|\nabla \mathbf{v}(x,y)|^2 + \frac{1}{2}\epsilon|\mathbf{v}(x,y)|^2 & 1 \le \epsilon|z| \le 1+\epsilon \\ 0 & \epsilon|z| \ge 1+\epsilon\,. \end{cases}$$

Thus

$$a_0(\mathbf{v}^\epsilon, \mathbf{v}^\epsilon) - \int_\Omega |\nabla \mathbf{v}(x,y)|^2\,dx\,dy = \int_{\frac{1}{\epsilon} \le |z| \le \frac{1}{\epsilon}+1} \int_\Omega |\nabla \mathbf{v}^\epsilon(x,y)|^2\,dx\,dy\,dz.$$

Therefore

$$\left| a_0(\mathbf{v}^\epsilon, \mathbf{v}^\epsilon) - \int_\Omega |\nabla \mathbf{v}(x,y)|^2\,dx\,dy \right| \le \epsilon \int_\Omega |\nabla \mathbf{v}(x,y)|^2 + |\mathbf{v}(x,y)|^2\,dx\,dy \le C\epsilon, \tag{108}$$

where C depends only on $\mathbf{v}$. Similarly,

$$\left| \mathcal{B}_0(\mathbf{v}^\epsilon, \mathbf{v}^\epsilon) - \int_\Omega 2v_x v_y b(x,y)\,dx\,dy \right| \le \epsilon \int_\Omega |b(x,y)|\,|\mathbf{v}(x,y)|^2\,dx\,dy \le C\epsilon, \tag{109}$$

where C depends only on $\mathbf{v}$ and b. Choose C to be the larger of the constants in (108) and (109). Then for ϵ sufficiently small,

$$\begin{aligned} \lambda_0^3 &\le \frac{\mathcal{B}_0(\mathbf{v}^\epsilon, \mathbf{v}^\epsilon)}{a_0(\mathbf{v}^\epsilon, \mathbf{v}^\epsilon)} \le \frac{\int_\Omega 2v_x v_y b(x,y)\,dx\,dy + C\epsilon}{\int_\Omega |\nabla \mathbf{v}(x,y)|^2\,dx\,dy - C\epsilon} \\ &\le \frac{\int_\Omega 2v_x v_y b(x,y)\,dx\,dy}{\int_\Omega |\nabla \mathbf{v}(x,y)|^2\,dx\,dy} + C'\epsilon, \end{aligned} \tag{110}$$

where C' depends only on C and $\mathbf{v}$. Since $\epsilon > 0$ was arbitrary, we conclude that

$$\lambda_0^3 \le \frac{\int_\Omega 2v_x v_y b(x,y)\,dx\,dy}{\int_\Omega |\nabla \mathbf{v}(x,y)|^2\,dx\,dy}. \tag{111}$$

Since $\mathbf{v} \in V_2^2$ was arbitrary, (91) implies

$$\lambda_0^3 \le \lambda^2. \tag{112}$$

Combining (112) and (106), we have proved the following result.

Theorem 11.2 *Suppose that $\mathcal{B}_0(\cdot,\cdot)$ is of the form (84). Let λ^2 be the most negative eigenvalue for the two-dimensional eigenvalue problem (91), and let λ_L^3 be the most negative eigenvalue for the three-dimensional eigenvalue problem (100). If $\lambda^2 \leq 0$, then*

$$\lambda^2 = \lambda_0^3.$$

That is, the three-dimensional problem cannot yield a lower eigenvalue.

11.4 Not all perturbations are 2D

Let us emphasize that the assumption (84) is essential in Theorems 11.1 and 11.2. By contrast, if

$$\nabla \mathbf{u} + \nabla \mathbf{u}^t = \begin{pmatrix} 1 & 0 & 0 \\ 0 & -1 & 0 \\ 0 & 0 & 0 \end{pmatrix} \tag{113}$$

then

$$\mathcal{B}_{\mathbf{u}}(\mathbf{v},\mathbf{v}) = \int_\Omega v_x^2 - v_y^2 \, d\mathbf{x}. \tag{114}$$

For any two-dimensional, divergence-free vector field $\mathbf{v} = (\psi_{,y}, -\psi_{,x}, 0)$, we would have

$$\mathcal{B}_{\mathbf{u}}(\mathbf{v},\mathbf{v}) = \int_\Omega \psi_{,y}^2 - \psi_{,x}^2 \, d\mathbf{x}.$$

In this case, it suggests that we should take ψ with small variation in y, which would mean v_x would be nearly constant. On the other hand, a vector field $\mathbf{v} = (0, \psi_{,z}, -\psi_{,y})^t$ has

$$\mathcal{B}_{\mathbf{u}}(\mathbf{v},\mathbf{v}) = \int_\Omega -\psi_{,z}^2 \, d\mathbf{x},$$

which is consistently negative. This three-dimensional perturbation can then have a significant contribution to instability for flows of the form (113).

It is interesting to examine the three-dimensional perturbation $\mathbf{v} = (0, \psi_{,z}, -\psi_{,y})^t$ for the Couette problem:

$$\begin{pmatrix} 0 \\ \psi_{,z} \\ -\psi_{,y} \end{pmatrix}^t \begin{pmatrix} 0 & 1 & 0 \\ 1 & 0 & 0 \\ 0 & 0 & 0 \end{pmatrix} \begin{pmatrix} 0 \\ \psi_{,z} \\ -\psi_{,y} \end{pmatrix} = \begin{pmatrix} 0 \\ \psi_{,z} \\ -\psi_{,y} \end{pmatrix}^t \begin{pmatrix} \psi_{,z} \\ 0 \\ 0 \end{pmatrix} = 0. \tag{115}$$

Similarly a vector field $\mathbf{v} = (\psi_{,z}, 0, -\psi_{,x})^t$ has

$$\begin{pmatrix} \psi_{,z} \\ 0 \\ -\psi_{,x} \end{pmatrix}^t \begin{pmatrix} 0 & 1 & 0 \\ 1 & 0 & 0 \\ 0 & 0 & 0 \end{pmatrix} \begin{pmatrix} \psi_{,z} \\ 0 \\ -\psi_{,x} \end{pmatrix} = \begin{pmatrix} \psi_{,z} \\ 0 \\ -\psi_{,x} \end{pmatrix}^t \begin{pmatrix} 0 \\ \psi_{,z} \\ 0 \end{pmatrix} = 0. \tag{116}$$

Thus neither of these three-dimensional perturbations play a role in Couette flow.

11.5 Representation for V_2^3

Although it does not play a role in our proof of Theorems 11.1 and 11.2, it is useful to know whether or not the representation of a divergence-free vector field with only two components is still a two-dimensional curl of a scalar-valued function. For functions in V_2^3, there is a simple representation.

Lemma 11.2 *Functions $\mathbf{v} \in V_2^3$ are of the form $\mathbf{v} = (\psi_{,y}, -\psi_{,x}, 0)$ for suitable ψ.*

Proof. While this is obvious for $\mathbf{v}$ independent of z, it requires justification when $\mathbf{v}$ depends on z. Since $\nabla\cdot\,\mathbf{v} = 0$, we know that $\mathbf{v} = \nabla \times \mathbf{w}$:

$$\begin{aligned}\mathbf{v} = (v_x, v_y, 0) = \nabla \times \mathbf{w} &= \det \begin{pmatrix} \mathbf{i} & \mathbf{j} & \mathbf{k} \\ \partial_x & \partial_y & \partial_z \\ w_x & w_y & w_z \end{pmatrix} \\ &= \mathbf{i}(w_{z,y} - w_{y,z}) + \mathbf{j}(w_{x,z} - w_{z,x}) + \mathbf{k}(w_{y,x} - w_{x,y}) \\ &= (w_{z,y}, -w_{z,x}, 0) - (w_{y,z}, -w_{x,z}, 0).\end{aligned} \tag{117}$$

Since $v_z = 0$, we must have $w_{y,x} = w_{x,y}$, which means that the vector field (w_x, w_y) is a gradient:

$$\widehat{\mathbf{w}} = (w_x, w_y) = \nabla_{x,y}\phi, \tag{118}$$

for each z. Thus

$$(w_{y,z}, -w_{x,z}, 0) = (\phi_{,zy}, -\phi_{,zx}, 0).$$

Therefore

$$\mathbf{v} = (v_x, v_y, 0) = (\psi_{,y}, -\psi_{,x}, 0), \quad \text{where } \psi = w_z - \phi_{,z}.$$

However, both w_z and ϕ can depend on z.

To clarify the existence of ϕ as claimed in (118), we modify the standard proof and define $\phi(0, 0, z) = 0$ and

$$\phi(x, y, z) = \int_0^1 (x, y) \cdot \widehat{\mathbf{w}}(tx, ty, z)\, dt. \tag{119}$$

Here we are making the simplifying assumption that Ω is star-shaped with respect to the origin $\mathbf{0}$. For a more complex domain, the integration path would need to be more complicated. With the definition (119), we find

$$\begin{aligned}\phi_{,x}(x, y, z) &= \int_0^1 w_x(tx, ty, z) + xtw_{x,x}(tx, ty, z) + ytw_{y,x}(tx, ty, z)\, dt \\ &= \int_0^1 w_x(tx, ty, z) + xtw_{x,x}(tx, ty, z) + ytw_{x,y}(tx, ty, z)\, dt \\ &= \int_0^1 \frac{\partial}{\partial t}\big(tw_x(tx, ty, z)\big)\, dt = w_x(x, y, z).\end{aligned} \tag{120}$$

Similarly, we can prove that $\phi_{,y}(x, y, z) = w_y(x, y, z)$. This completes the proof of Lemma 11.2.

12 Bounds for Couette perturbations

A general solution $\mathbf{w}$ of (4) for the domain (2) and with boundary conditions $\mathbf{g}$ in (3) satisfies certain bounds that limit the global growth of the perturbed solutions. Multiply (4) by $\mathbf{w}$ (dot product), integrate over Ω, and integrate by parts to get

$$\begin{aligned}\frac{1}{2}\frac{\partial}{\partial t}\|\mathbf{w}\|^2_{L^2(\Omega)} + \nu\int_\Omega |\nabla\mathbf{w}|^2\,d\mathbf{x} &= \nu\oint_{\partial\Omega}\mathbf{n}\cdot\left((\nabla\mathbf{w})^t\mathbf{g}\right)ds \\ &= \nu\oint_{\partial\Omega}\mathbf{n}\cdot\left((\nabla\mathbf{g})^t\mathbf{g}\right)ds + \nu\oint_{\partial\Omega}\mathbf{n}\cdot\left((\nabla\mathbf{v})^t\mathbf{g}\right)ds.\end{aligned} \tag{121}$$

The first boundary integral in (121) can be evaluated since

$$(\nabla\mathbf{g})^t\mathbf{g} = \begin{pmatrix}0 & 0\\ 1 & 0\end{pmatrix}\begin{pmatrix}y-\frac{1}{2}\\ 0\end{pmatrix} = \begin{pmatrix}0\\ y-\frac{1}{2}\end{pmatrix}.$$

Thus

$$\mathbf{n}\cdot(\nabla\mathbf{g})^t\mathbf{g} = \begin{cases}\frac{1}{2} & \text{top and bottom of } \partial\Omega\\ 0 & \text{inlet and outlet of } \partial\Omega.\end{cases}$$

Therefore

$$\oint_{\partial\Omega}\mathbf{n}\cdot\left((\nabla\mathbf{g})^t\mathbf{g}\right)ds = 2L = \int_\Omega 1\,d\mathbf{x}.$$

Thus

$$\frac{1}{2}\frac{\partial}{\partial t}\|\mathbf{w}\|^2_{L^2(\Omega)} + \nu\int_\Omega\left(|\nabla\mathbf{w}|^2-1\right)d\mathbf{x} = \nu\oint_{\partial\Omega}\mathbf{n}\cdot\left((\nabla\mathbf{v})^t\mathbf{g}\right)ds. \tag{122}$$

Ignoring the small term involving $\mathbf{v}$, this says that $\|\mathbf{w}\|_{L^2(\Omega)}$ can grow only when $|\nabla\mathbf{w}| < 1$. This seem contradictory, but in fact it describes something like a governor on a motor. If it goes too fast, it slows down. Note that $|\nabla\mathbf{g}| = 1$.

The expression (122) can be modified as follows. First of all

$$|\nabla\mathbf{w}|^2 - 1 = |\nabla(\mathbf{v}+\mathbf{g})|^2 - 1 = |\nabla\mathbf{v}|^2 + 2\nabla\mathbf{v}\cdot\nabla\mathbf{g}.$$

But

$$\int_\Omega \nabla\mathbf{v}\cdot\nabla\mathbf{g}\,d\mathbf{x} = \int_\Omega v_{x,y}\,d\mathbf{x} = 0$$

since $\mathbf{v}$ is zero on $\partial\Omega$. Similarly

$$\frac{\partial}{\partial t}\|\mathbf{w}\|^2_{L^2(\Omega)} = \frac{\partial}{\partial t}\|\mathbf{v}+\mathbf{g}\|^2_{L^2(\Omega)} = \frac{\partial}{\partial t}\|\mathbf{v}\|^2_{L^2(\Omega)} + 2\int_\Omega \mathbf{v}_t\cdot\mathbf{g}\,d\mathbf{x}.$$

Thus expression (122) becomes

$$\frac{1}{2}\frac{\partial}{\partial t}\|\mathbf{v}\|^2_{L^2(\Omega)} + \int_\Omega \mathbf{v}_t\cdot\mathbf{g}\,d\mathbf{x} + \nu\int_\Omega|\nabla\mathbf{v}|^2\,d\mathbf{x} = \nu\oint_{\partial\Omega}\mathbf{n}\cdot\left((\nabla\mathbf{v})^t\mathbf{g}\right)ds. \tag{123}$$

The derivation of (121) stems from the divergence theorem

$$\int_\Omega \nabla\cdot \mathbf{w}\, d\mathbf{x} = \oint_{\partial\Omega} \mathbf{w}\cdot\mathbf{n}\, ds,$$

applied to $\mathbf{w} = (\nabla\mathbf{u})^t\mathbf{v}$, and using the formula

$$\nabla\cdot\left((\nabla\mathbf{u})^t\mathbf{v}\right) = (\Delta\mathbf{u})\cdot\mathbf{v} + \nabla\mathbf{u} : \nabla\mathbf{v}. \tag{124}$$

To prove (124), we expand using indices:

$$\begin{aligned}\nabla\cdot\left((\nabla\mathbf{u})^t\mathbf{v}\right) &= \sum_i \left((\nabla\mathbf{u})^t\mathbf{v}\right)_{i,i} = \sum_{ij}(u_{j,i}v_j)_{,i} \\ &= \sum_{ij}\left(u_{j,ii}v_j + u_{j,i}v_{j,i}\right) = (\Delta\mathbf{u})\cdot\mathbf{v} + \nabla\mathbf{u} : \nabla\mathbf{v}.\end{aligned} \tag{125}$$

Thus

$$\int_\Omega (\Delta\mathbf{u})\cdot\mathbf{v} + \nabla\mathbf{u} : \nabla\mathbf{v}\, d\mathbf{x} = \oint \mathbf{n}\cdot(\nabla\mathbf{u})^t\mathbf{v}\, ds,$$

and so

$$-\int_\Omega (\Delta\mathbf{u})\cdot\mathbf{v}\, d\mathbf{x} = \int_\Omega \nabla\mathbf{u} : \nabla\mathbf{v}\, d\mathbf{x} - \oint \mathbf{n}\cdot(\nabla\mathbf{u})^t\mathbf{v}\, ds,$$

confirming (121).

13 Conclusions

We have utilized a technique to predict instability of a given fluid flow profile. It involves solving a symmetric eigenproblem. It rigorously identifies a mode leading to a growth in amplitude of kinetic energy due to a perturbation to the given flow. We have applied the technique to Couette flow and have predicted a critical Reynolds number above which such instability can occur. For even larger Reynolds numbers, additional unstable modes may appear, identified as eigenvectors of the eigenproblem we describe. Thus for very high Reynolds numbers, there could be a very high-dimensional space of perturbations that lead to energy instability.

For Couette flow, we have also investigated how the most unstable mode grows or decays, depending on Reynolds number, by solving the time-dependent Navier-Stokes equations with perturbed initial values. We have seen that the perturbations grow in time at a rate that increases as the Reynolds number increases. Moreover, they reach a greater magnitude and remain persistent for longer times for larger Reynolds numbers.

14 Future Research

We can extend the basic results developed here in many directions. Potential flow provides an exact, steady solution of the Navier-Stokes equations, independent of the Reynolds

number, with slip ($\mathbf{u} \cdot \mathbf{n} = 0$) boundary conditions, with suitable friction coefficient. We are extending the results derived here to slip boundary conditions, with application to flow around a cylinder [12], where (113) holds instead of (84). Boundary-layer flow is very similar to Couette flow in mathematical structure, in particular satisfying (84), as we show in a companion paper.

Despite our identification of energy-unstable modes, as well as the rate of their initial growth in kinetic energy, we cannot say in general how much growth ultimately occurs. Although we have given examples for Couette flow, we do not have a general theory to predict the ultimate fate of the unstable modes. The identified perturbations may in some cases quickly dissipate. Nor can we say how likely such a perturbation is to occur. Thus further study is required to understand the physical implications of the unstable modes. In fact, what we have *not* done so far is multifactorial. In addition to the growth and likelihood questions, we introduce some more precise questions as follows.

1. What is the most unstable mode for plane Poiseuille flow and pipe flow? How does this compare with the mode found by Orszag [29]?

2. The original experiments of Couette were done using concentric, counter-rotating cylinders, with fluid in between the cylinders. What is the most unstable mode for such a flow domain?

3. A low-frequency instability has been observed [13, 38] in pipe flow that interacts with high frequency perturbations in a feed-back loop. Can energy instability explain this in any way?

4. For the most unstable mode, exactly how does the perturbation grow in time for Couette flow? For other flows?

5. How many eigenvalues are there satisfying (35)? What do the eigenfunctions look like? This question applies to all flow problems, but begin with Couette.

6. Experiments [40] and simulations [26] have observed instabilities in Couette flow for $R \approx 1600$, about eight times higher than for our observed most energy-unstable mode. Can this discrepancy be explained by other eigenvalues satisfying (35)? Or is there a threshold where the rate of growth r defined in (33) must be sufficiently high for the instability to be observed on the relevant time scales?

7. In more complex flow geometries, the solution $\mathbf{u}$ depends on the Reynolds number R, so statements about instabilities will be different. The question is about stability of a solution $\mathbf{u}_R$ that depends on R, and there will be a resulting eigenvalue λ_R corresponding to the most unstable mode. Then the condition for instability is $-\lambda_R > 2/R$. If this holds for one R, then by continuity it probably holds for an interval of R values, but this interval does not need to be infinite in extent as it is in the Couette flow case. The simplest such system might be flow in a sudden expansion. For R sufficiently large, there are multiple solutions, after a pitchfork bifurcation [36] at $R = R_0$. Is there an energy instability for a smaller value of $R < R_0$? For $R > R_0$? How does the most

unstable mode depend on R? Begin initially with a two-dimensional problem and then see how this changes with three-dimensional versions as described previously for Couette flow. Check to see if (84) holds.

8. What about airfoils? First consider two-dimensional problems as done here for Couette flow. How different are three-dimensional problems in which we allow three-dimensional perturbations?

9. Do energy instabilities relate in any way to the drag crisis [16]?

10. It appears from our computations that the most unstable mode for Couette flow is essentially periodic in the streamwise (horizontal) flow direction. What if we pose the problem as periodic in this direction, with period p, and we compute λ_p. What value of p minimizes λ_p?

11. It appears from our computations that the lowest eigenvalue λ defined in (15) is simple for Couette flow. Can this be proved?

15 Acknowledgments

We thank Patrick Farrell, Ingeborg Gjerde, Chiara Giraudo, Matt Knepley, Mats Larson, Maureen Morton, Leo Rebholz, and Nick Trefethen for valuable suggestions. Our understanding of this subject was enhanced substantially by the book [17].

References

[1] James P. Abbott. An efficient algorithm for the determination of certain bifurcation points. *Journal of Computational and Applied Mathematics*, 4(1):19–27, 1978.

[2] Martin Alnæs, Jan Blechta, Johan Hake, August Johansson, Benjamin Kehlet, Anders Logg, Chris Richardson, Johannes Ring, Marie E. Rognes, and Garth N. Wells. The FEniCS project version 1.5. *Archive of Numerical Software*, 3(100), 2015.

[3] Jacob Bedrossian, Pierre Germain, and Nader Masmoudi. Stability of the Couette flow at high Reynolds numbers in two dimensions and three dimensions. *Bulletin of the American Mathematical Society*, 56(3):373–414, 2019.

[4] Susanne C. Brenner and L. Ridgway Scott. *The Mathematical Theory of Finite Element Methods*. Springer-Verlag, third edition, 2008.

[5] Eric Cancès and L. Ridgway Scott. van der Waals interactions between two hydrogen atoms: The Slater-Kirkwood method revisited. *SIAM Journal on Mathematical Analysis*, 50(1):381–410, 2018.

[6] Subrahmanyan Chandrasekhar. *Hydrodynamic and Hydromagnetic Stability*. New York: Dover Publications, 1981.

[7] K. Andrew Cliffe, Edward J. C. Hall, Paul Houston, Eric T. Phipps, and Andrew G. Salinger. Adaptivity and a posteriori error control for bifurcation problems III: Incompressible fluid flow in open systems with $O(2)$ symmetry. *Journal of Scientific Computing*, 52(1):153–179, 2012.

[8] Michael G. Crandall and Paul H. Rabinowitz. Bifurcation from simple eigenvalues. *Journal of Functional Analysis*, 8(2):321–340, 1971.

[9] F. Daviaud, J. Hegseth, and P. Bergé. Subcritical transition to turbulence in plane Couette flow. *Physical review letters*, 69(17):2511, 1992.

[10] H. S. Dou, B. C. Khoo, N. Phan-Thien, and K. S. Yeo. Instability of plane Couette flow. Technical report, Technical Report, National University of Singapore, 2003.

[11] Howard C. Elman and David J. Silvester. Collocation methods for exploring perturbations in linear stability analysis. *SIAM Journal on Scientific Computing*, 40(4):A2667–A2693, 2018.

[12] Ingeborg Gjerde and L. Ridgway Scott. Kinetic-energy instability of flows with slip boundary conditions. *TBD*, ?:??, 2021.

[13] Nigel Goldenfeld and Hong-Yan Shih. Turbulence as a problem in non-equilibrium statistical mechanics. *Journal of Statistical Physics*, 167(3-4):575–594, 2017.

[14] Ben-yu Guo, Jie Shen, and Cheng-long Xu. Spectral and pseudospectral approximations using Hermite functions: application to the Dirac equation. *Advances in Computational Mathematics*, 19(1-3):35–55, 2003.

[15] Werner Heisenberg. *On Stability and Turbulence of Fluid Flows*. Technical memorandums/National Advisory Committee for Aeronautics; no. 1291. U.S. Federal Government Document, Book, E-Resource, 1951.

[16] Johan Hoffman. Simulation of turbulent flow past bluff bodies on coarse meshes using General Galerkin methods: drag crisis and turbulent Euler solutions. *Computational Mechanics*, 38(4-5):390–402, 2006.

[17] Johan Hoffman and Claes Johnson. *Computational Turbulent Incompressible Flow*. Springer Science & Business Media, 2007.

[18] Daniel D. Joseph. *Stability of Fluid Motions I*, volume 27. Springer Science & Business Media, 2013.

[19] Daniel D. Joseph. *Stability of Fluid Motions II*, volume 28. Springer Science & Business Media, 2013.

[20] R. R. Kerswell. Nonlinear nonmodal stability theory. *Annual Review of Fluid Mechanics*, 50:319–345, 2018.

[21] Joseph Kestin, Mordechai Sokolov, and William A Wakeham. Viscosity of liquid water in the range −8 C to 150 C. *Journal of Physical and Chemical Reference Data*, 7(3):941–948, 1978.

[22] F. Lam. Stability of the Couette-Poiseuille flow by the Reynolds-Orr energy equation. *arXiv preprint arXiv:1210.1327*, 2012.

[23] Adam Larios, Leo G. Rebholz, and Camille Zerfas. Global in time stability and accuracy of IMEX-FEM data assimilation schemes for Navier–Stokes equations. *Computer Methods in Applied Mechanics and Engineering*, 345:1077–1093, 2019.

[24] C. C. Lin. *The Theory of Hydrodynamic Stability.* Cambridge University Press, Cambridge, 1955.

[25] Jianzhou Lu, Jianjun Tao, Weitao Zhou, and Xiangming Xiong. Threshold and decay properties of transient isolated turbulent band in plane Couette flow. *Applied Mathematics and Mechanics*, 40(10):1449–1456, 2019.

[26] Anders Lundbladh and Arne V. Johansson. Direct simulation of turbulent spots in plane Couette flow. *Journal of Fluid Mechanics*, 229:499–516, 1991.

[27] D. S. Malkus and E. T. Olsen. Linear crossed triangles for incompressible media. *North-Holland Mathematics Studies*, 94:235–248, 1984.

[28] William M'F Orr. The stability or instability of the steady motions of a perfect liquid and of a viscous liquid. Part II: A viscous liquid. *Proceedings of the Royal Irish Academy. Section A: Mathematical and Physical Sciences*, pages 69–138, 1907.

[29] Steven A. Orszag. Accurate solution of the Orr–Sommerfeld stability equation. *Journal of Fluid Mechanics*, 50(4):689–703, 1971.

[30] Arnaud Prigent, Guillaume Grégoire, Hugues Chaté, and Olivier Dauchot. Long-wavelength modulation of turbulent shear flows. *Physica D: Nonlinear Phenomena*, 174(1-4):100–113, 2003.

[31] Eyvind Riis. *The Stability of Couette-flow in Non-stratified and Stratified Viscous Fluids.* Oslo: Universitetsforlaget, 1962.

[32] V. A. Romanov. Stability of plane-parallel Couette flow. *Functional Analysis and Its Applications*, 7(2):137–146, 1973.

[33] Margarete Sandelowski. Rigor or rigor mortis: the problem of rigor in qualitative research. *Advances in Nursing Science*, 16(2):1–8, 1993.

[34] Peter J. Schmid and Dan S. Henningson. *Stability and Transition in Shear Flows*. Applied Mathematical Sciences, Vol. 142. Springer, 2001.

[35] L. Ridgway Scott. *Numerical Analysis*. Princeton Univ. Press, 2011.

[36] L. Ridgway Scott. *Introduction to Automated Modeling with FEniCS*. Computational Modeling Initiative, 2018.

[37] James Serrin. On the stability of viscous fluid motions. *Archive for Rational Mechanics and Analysis*, 3(1):1–13, 1959.

[38] Hong-Yan Shih, Tsung-Lin Hsieh, and Nigel Goldenfeld. Ecological collapse and the emergence of travelling waves at the onset of shear turbulence. *Nature Physics*, 12(3):245, 2016.

[39] Geoffrey Ingram Taylor. VIII. Stability of a viscous liquid contained between two rotating cylinders. *Philosophical Transactions of the Royal Society of London. Series A, Containing Papers of a Mathematical or Physical Character*, 223(605-615):289–343, 1923.

[40] Nils Tillmark and P. Henrik Alfredsson. Experiments on transition in plane Couette flow. *Journal of Fluid Mechanics*, 235:89–102, 1992.

[41] Lloyd N. Trefethen and Mark Embree. *Spectra and Pseudospectra: the Behavior of Nonnormal Matrices and Operators*. Princeton University Press, 2005.

[42] Lloyd N. Trefethen, Anne E. Trefethen, Satish C. Reddy, and Tobin A. Driscoll. Hydrodynamic stability without eigenvalues. *Science*, 261(5121):578–584, 1993.

[43] Laurette S. Tuckerman, Matthew Chantry, and Dwight Barkley. Patterns in wall-bounded shear flows. *Annual Review of Fluid Mechanics*, 52, 2020.

[44] Fabian Waleffe. On a self-sustaining process in shear flows. *Physics of Fluids*, 9(4):883–900, 1997.